

Resolving the fibrotic niche of human liver cirrhosis at single cell level

Ramachandran P^{1*}, Dobie R¹, Wilson-Kanamori JR¹, Dora EF¹, Henderson BEP¹, Luu NT^{2,3}, Portman JR¹, Matchett KP¹, Brice M¹, Marwick JA^{1,4}, Taylor RS¹, Efremova M⁵, Vento-Tormo R⁵, Carragher NO⁴, Kendall TJ^{1,6}, Fallowfield JA¹, Harrison EM⁷, Mole DJ^{1,7}, Wigmore SJ^{1,7}, Newsome PN^{2,3}, Weston CJ^{2,3}, Iredale JP⁸, Tacke F⁹, Pollard JW^{10,11}, Ponting CP¹², Marioni JC^{5,13,14}, Teichmann SA^{5,13,15}, Henderson NC^{1*}

¹University of Edinburgh Centre for Inflammation Research, The Queen's Medical Research Institute, Edinburgh BioQuarter, Edinburgh, UK.

²NIHR Birmingham Biomedical Research Centre, University Hospitals Birmingham NHS Foundation Trust and University of Birmingham, UK

³Institute of Immunology and Immunotherapy, University of Birmingham, UK

⁴Cancer Research UK Edinburgh Centre, MRC Institute of Genetics and Molecular Medicine at the University of Edinburgh, Edinburgh, UK.

⁵Wellcome Sanger Institute, Wellcome Genome Campus, Hinxton, Cambridge, UK.

⁶Division of Pathology, University of Edinburgh, Edinburgh, UK.

⁷Clinical Surgery, University of Edinburgh, Royal Infirmary of Edinburgh, Edinburgh, UK.

⁸Office of the Vice Chancellor, Beacon House and National Institute for Health Research, Biomedical Research Centre, Bristol, UK

⁹Department of Hepatology and Gastroenterology, Charité University Medical Center, Berlin, Germany

¹⁰MRC Centre for Reproductive Health, The Queen's Medical Research Institute, University of Edinburgh, Edinburgh, UK.

¹¹Department of Developmental and Molecular Biology, Albert Einstein College of Medicine, New York, USA.

¹²MRC Human Genetics Unit, MRC Institute of Genetics and Molecular Medicine at the University of Edinburgh, Edinburgh, UK.

¹³European Molecular Biology Laboratory, European Bioinformatics Institute (EMBL-EBI), Hinxton, Cambridge, UK.

¹⁴Cancer Research UK Cambridge Institute, University of Cambridge, Li Ka Shing Centre, Cambridge, UK.

¹⁵Theory of Condensed Matter Group, The Cavendish Laboratory, University of Cambridge, JJ Thomson Ave, Cambridge, CD3 0EH, UK.

*Address correspondence to:

Prakash Ramachandran, University of Edinburgh Centre for Inflammation Research, The Queen's Medical Research Institute, Edinburgh BioQuarter, 47 Little France Crescent, Edinburgh, UK, EH16 4TJ. Phone: 0131.242.6654; Email: Prakash.Ramachandran@ed.ac.uk or Neil Henderson, University of Edinburgh Centre for Inflammation Research, The Queen's Medical Research Institute, Edinburgh BioQuarter, 47 Little France Crescent, Edinburgh, UK, EH16 4TJ. Phone: 0131.242.6688; Email: Neil.Henderson@ed.ac.uk

1 **Abstract**

2 Currently there are no effective antifibrotic therapies for liver cirrhosis, a major killer
3 worldwide. To obtain a cellular resolution of directly-relevant pathogenesis and to
4 inform therapeutic design, we profile the transcriptomes of over 100,000 human single
5 cells, yielding molecular definitions for non-parenchymal cell types present in healthy
6 and cirrhotic human liver. We uncover a novel scar-associated TREM2⁺CD9⁺
7 macrophage subpopulation, which expands in liver fibrosis, differentiates from
8 circulating monocytes and is pro-fibrogenic. We also define novel ACKR1⁺ and
9 PLVAP⁺ endothelial cells which expand in cirrhosis, are topographically scar-restricted
10 and enhance leucocyte transmigration. Multi-lineage ligand-receptor modelling of
11 interactions between the novel scar-associated macrophages, endothelial cells and
12 PDGFR α ⁺ collagen-producing mesenchymal cells reveals intra-scar activity of several
13 pro-fibrogenic pathways including TNFRSF12A, PDGFR and NOTCH signalling. Our
14 work dissects unanticipated aspects of the cellular and molecular basis of human organ
15 fibrosis at a single-cell level, and provides the conceptual framework required to
16 discover rational therapeutic targets in liver cirrhosis.

17 **Main**

18 Recent estimates suggest that 844 million people worldwide have chronic liver disease,
19 with two million deaths per year and a rising incidence¹. Iterative liver injury secondary
20 to any cause leads to progressive fibrosis ultimately resulting in liver cirrhosis.
21 Importantly, the degree of liver fibrosis predicts adverse patient outcomes². Hence,
22 effective antifibrotic therapies for patients with chronic liver disease are urgently
23 required^{3,4}.

24 Liver fibrosis involves a complex interplay between multiple non-parenchymal cell
25 (NPC) lineages including immune, endothelial and mesenchymal cells spatially located
26 within areas of scarring, termed the fibrotic niche. Despite progress in our
27 understanding of liver fibrogenesis accrued using rodent models, there remains a
28 significant 'translational gap' between putative targets and effective patient therapies^{3,4}.
29 This is in part due to limited definition of the functional heterogeneity and interactome
30 of cell lineages that contribute to the fibrotic niche of human liver cirrhosis, which is
31 imperfectly recapitulated by rodent models³.

32 Single-cell RNA sequencing (scRNA-seq) is delivering a step change in our
33 understanding of disease pathogenesis, allowing the interrogation of individual cell
34 populations at unprecedented resolution⁵. Here, we studied the mechanisms regulating
35 human liver fibrosis using scRNA-seq.

36 **Results**

37 **Single-cell atlas of human liver NPC**

38 Hepatic NPC were isolated from healthy and cirrhotic human livers spanning a range
39 of aetiologies of cirrhosis (Fig. 1a, Extended Data Fig. 1a). Leucocytes (CD45⁺) or
40 other NPC (CD45⁻) fractions (Extended Data Fig. 1b) were FACS-sorted prior to
41 scRNA-seq. To discriminate between liver-resident and circulating leucocytes, we also
42 performed scRNA-seq on CD45⁺CD66b⁻ peripheral blood mononuclear cells (PBMC)
43 (Extended Data Fig. 1c, g-i). The combined tissue and PBMC dataset was partitioned
44 into clusters (Extended Data Fig. 1d) and annotated using signatures of known lineage

45 markers (Extended Data Fig. 1d-e; Supplementary Table 2). To generate an atlas of
46 liver-resident cells, contaminating circulating cells were removed from the liver tissue
47 datasets, by excluding cells from the tissue samples which mapped transcriptionally to
48 blood-derived clusters 1 and 13 (Extended Data Fig. 1d). Liver-resident cells expressed
49 higher levels of tissue-residency markers such as CXCR4 compared to PBMC
50 (Extended Data Fig. 1f).

51 Re-clustering the 66,135 liver-resident cells from 10 livers (n=5 healthy and n=5
52 cirrhotic) revealed 21 populations (Fig. 1b), each containing cells from both healthy
53 and cirrhotic livers (Fig. 1c; Extended Data Fig. 2), across 10 cell lineages (Fig. 1d,
54 Extended Data Fig. 2a, b). Subpopulation markers were identified across all clusters
55 and lineages (Fig. 1e; Supplementary Tables 3, 4). QC metrics were highly reproducible
56 between individual samples and condition (Extended Data Fig. 2c-f, Supplementary
57 Table 1). Expression of collagens type I and III, the main fibrillar collagens within the
58 fibrotic niche, was restricted to cells of the mesenchymal lineage (Fig. 1e).

59 We proceeded to annotate all human liver NPC lineages (below, Supplementary Notes
60 1-3, Extended Data Fig. 3), and provide an open-access gene browser
61 (<http://www.livercellatlas.mvm.ed.ac.uk>) allowing assessment of NPC gene expression
62 between healthy and cirrhotic livers.

63 **Distinct macrophage subpopulations inhabit the fibrotic niche**

64 Previous studies in rodents have highlighted macrophage subpopulations orchestrating
65 both liver fibrosis progression and regression⁶⁻⁸. Clustering of mononuclear phagocytes
66 (MP) identified ten clusters; annotated as scar-associated macrophages (SAM Φ),
67 Kupffer cells (KC), tissue monocytes (TMO), conventional dendritic cells (cDC) and
68 cycling (proliferating) cells (Fig. 2a, Extended Data Fig. 4a, Supplementary Note 2).
69 Clusters MP(4) and MP(5), named SAM Φ (1) and SAM Φ (2) respectively, were
70 expanded in cirrhotic livers (Fig. 2b), as confirmed by quantification of the MP cell
71 composition of each liver individually (Fig. 2c).

72 Clusters MP(6) and MP(7) were enriched in *CD163*, *MARCO* and *TIMD4* (Extended
73 Data Fig. 4b); tissue staining confirmed these as Kupffer cells (KC; resident liver

74 macrophages), facilitating annotation of these clusters as KC(1) and KC(2) respectively
75 (Extended Data Fig. 4c). A lack of *TIMD4* expression distinguished KC(2) from KC(1)
76 (Extended Data Fig. 4b); cell counting demonstrated *TIMD4*⁺ cell numbers to be
77 equivalent between healthy and cirrhotic livers, but showed a loss of *MARCO*⁺ cells,
78 consistent with selective reduction in *MARCO*⁺*TIMD4*⁻ KC(2) in liver fibrosis (Fig.
79 2c, Extended Data Fig. 4d, e).

80 Scar-associated clusters *SAMΦ*(1) and *SAMΦ*(2) expressed the unique markers
81 *TREM2* and *CD9* (Fig. 2d, e). These macrophages displayed a hybrid phenotype, with
82 features of both tissue monocytes and KC (Fig. 2d, e), analogous to monocyte-derived
83 macrophages in murine liver injury models⁷. Flow cytometry confirmed expansion of
84 *TREM2*⁺*CD9*⁺ macrophages in human fibrotic livers (Fig. 2f, Extended Data Fig. 4f).
85 Conditioned media from FACS-sorted *SAMΦ* promoted fibrillar collagen expression
86 by primary human hepatic stellate cells (HSC) (Fig. 2g), indicating that *SAMΦ* have a
87 pro-fibrogenic phenotype. Tissue staining demonstrated the presence of
88 *TREM2*⁺*CD9*⁺*MNDA*⁺ *SAMΦ* topographically localised in collagen-positive scar
89 regions (Fig. 2h, Extended Data Fig. 4g-i), and significantly expanded in cirrhotic livers
90 (Extended Data Fig. 4j, k). Cell counting of stained cirrhotic livers morphologically
91 segmented into regions of fibrotic septae and parenchymal nodules, confirmed *SAMΦ*
92 accumulation within the fibrotic niche (Extended Data Fig. 4l).

93 Local proliferation plays a significant role in macrophage expansion at sites of fibrosis
94 in rodent models^{7,9}. Cycling MP cells (Fig. 2a) subclustered into cDC1, cDC2, KC and
95 *SAMΦ* subpopulations (Extended Data Fig. 4m, Supplementary Table 8). Cycling
96 *SAMΦ* expanded in cirrhosis (Extended Data Fig. 4m), highlighting the potential role
97 of macrophage proliferation in promoting *SAMΦ* accumulation in the fibrotic niche.

98 **Pro-fibrogenic phenotype of scar-associated macrophages**

99 To delineate the functional profile of *SAMΦ* we visualised co-ordinately expressed
100 gene groups across the MP subpopulations using self-organising maps (Extended Data
101 Fig. 5a). We identified six optimally-differentiating metagene signatures, denoted as A-
102 F (Extended Data Fig. 5a, Supplementary Table 9). Signatures A and B defined *SAMΦ*
103 and were enriched for ontology terms relevant to tissue fibrosis (Extended Data Fig.

104 5b). These SAM Φ -defining signatures included genes such as *TREM2*, *IL1B*, *SPP1*,
105 *LGALS3*, *CCR2*, and *TNFSF12*, some of which are known to regulate the function of
106 scar-producing myofibroblasts in fibrotic liver diseases¹⁰⁻¹³. The remaining MP
107 subpopulations were defined by signature C (KC), signatures D, E (TMO) and signature
108 F (cDC1); ontology terms matched known functions for the associated cell type
109 (Extended Data Fig. 5b, Supplementary Table 9).

110 In mice, under homeostatic conditions, embryologically-derived self-renewing tissue-
111 resident KC predominate¹⁴⁻¹⁶. However, following injury, macrophages derived from
112 circulating monocytes accumulate in the liver and regulate fibrosis^{7,8}. The ontogeny of
113 human hepatic macrophage subpopulations is unknown. TREM2⁺CD9⁺ SAM Φ
114 demonstrated a monocyte-like morphology (Fig. 2h, Extended Data Fig. 4g-i) and a
115 distinct topographical distribution from KC (Extended Data Fig. 4l). To assess SAM Φ
116 origin, we performed *in silico* trajectory analysis on a combined dataset of peripheral
117 blood monocytes and liver-resident MPs. We visualised the transcriptional profile of
118 these cells (Fig. 3a, Extended Data Fig. 5c), mapped them along a pseudotemporal
119 trajectory and interrogated their directionality via spliced and unspliced mRNA ratios
120 (RNA velocity¹⁷). These analyses suggested a differentiation trajectory from peripheral
121 blood monocytes into either SAM Φ or cDC, with no differentiation from KC to SAM Φ ,
122 and no progression from SAM Φ to KC (Fig. 3a; Extended Data Fig. 5c). Additional
123 RNA velocity analyses¹⁷ showed downregulation (negative velocity) of the monocyte
124 gene *MNDA* in SAM Φ , upregulation (positive velocity) of the SAM Φ marker gene *CD9*
125 in tissue monocytes, and a lack of KC gene *TIMD4* velocity in SAM Φ (Extended Data
126 Fig. 5d). Furthermore, assessment of the probabilities of cells in this dataset
127 transitioning into SAM Φ , indicated a higher likelihood of tissue monocytes than KC
128 differentiating into SAM Φ (Fig. 3b). Overall, these data suggest that SAM Φ are
129 monocyte-derived, and represent a terminally-differentiated cell state within the fibrotic
130 niche.

131 To further characterise SAM Φ phenotype, we identified differentially expressed genes
132 along monocyte differentiation trajectories. We defined three gene co-expression
133 modules, with module 1 representing upregulated genes during blood monocyte-to-
134 SAM Φ differentiation (Fig. 3c). Module 1 contained multiple pro-fibrogenic genes

135 including *SPPI*, *LGALS3*, *CCL2*, *CXCL8*, *PDGFB* and *VEGFA*^{10–13}, and displayed
136 ontology terms consistent with promoting tissue fibrosis and angiogenesis (Fig. 3c, d;
137 Supplementary Table 10). Module 2 contained genes that were downregulated during
138 monocyte-to-SAM Φ differentiation (Fig. 3c; Extended Data Fig. 5e), whilst Module 3
139 encompassed a group of upregulated genes during monocyte-to-cDC differentiation
140 (Fig. 3c; Extended Data Fig. 5f; Supplementary Table 10). SAM Φ isolated from
141 cirrhotic human livers (Fig. 2f, Extended Data Fig. 4f) demonstrated enhanced protein
142 secretion of several of the mediators identified by transcriptional analysis (Extended
143 Data Fig. 5g) and promoted fibrillar collagen expression by primary human HSC (Fig.
144 2g), confirming that SAM Φ have a pro-fibrogenic phenotype.

145 To enable cross-species comparison, we performed scRNA-seq on liver MP cells
146 isolated from control mice or mice treated with chronic carbon tetrachloride (CCl₄), a
147 mouse model of liver fibrosis⁷. MP cells from fibrotic livers were isolated 24 hours
148 after the final CCl₄ injection, a time of active fibrogenesis⁷. Five MP cell clusters were
149 defined (Extended Data Fig. 6a-d, Supplementary Table 11), and injury-specific cluster
150 mMP(2) was differentiated by high expression of *Cd9*, *Trem2*, *Spp1* and *Lgals3*
151 (Extended Data Fig. 6a-d). We confirmed expansion of this CD9⁺ SAM Φ (mSAM Φ)
152 population in liver fibrosis (Extended Data Fig. 6e, f) and co-culture of mSAM Φ with
153 quiescent primary murine HSC promoted fibrillar collagen expression in HSC
154 (Extended Data Fig. 6g). Canonical correlation analysis between human and mouse MP
155 datasets¹⁸ demonstrated that human SAM Φ (hSAM Φ) and mSAM Φ clustered together
156 (h&mMP(2); Extended Data Fig. 6h, i) and that this cluster was enriched for SAM Φ
157 markers *CD9*, *TREM2* and *SPPI* (Extended Data Fig. 6j), confirming that mSAM Φ
158 represent a corollary population to human SAM Φ (hSAM Φ).

159 To identify potential transcriptional regulators of human SAM Φ we defined sets of
160 genes co-expressed with known transcription factors (regulons) along the tissue
161 monocyte-macrophage pseudotemporal trajectory and in KC (Extended Data Fig. 5g,
162 h, Supplementary Table 12). This identified regulons and corresponding transcription
163 factors associated with distinct macrophage phenotypes, highlighting *HES1* and *EGR2*
164 activity in SAM Φ .

165 To determine whether SAM Φ expand in earlier stage human liver disease, we analysed
166 cohorts of patients with non-alcoholic fatty liver disease (NAFLD). Application of
167 differential gene expression signatures of human SAM Φ , KC and TMo to a
168 deconvolution algorithm¹⁹ enabled assessment of hepatic monocyte-macrophage
169 composition in whole liver microarray data across the spectrum of early-stage
170 NAFLD²⁰ (Extended Data Fig. 7a). This demonstrated SAM Φ expansion in patients
171 with non-alcoholic steatohepatitis (NASH) (Extended Data Fig. 7a, b), an increased
172 frequency of SAM Φ with worsening histological NASH activity (NAS) and fibrosis
173 scores (Extended Data Fig. 7c), but no association with other patient demographics
174 (Extended Data Fig. 7d). In a separate NASH biopsy cohort, SAM Φ expansion
175 increased with NASH activity (Extended Data Fig. 7e) and positively correlated with
176 the degree of fibrosis across the full severity spectrum of NAFLD-induced liver fibrosis
177 (Extended Data Fig. 7f).

178 In summary, these data demonstrate that TREM2⁺CD9⁺ SAM Φ derive from the
179 recruitment and differentiation of circulating monocytes, are conserved across species,
180 display a pro-fibrogenic phenotype and expand early in the course of liver disease
181 progression.

182 **Distinct endothelial subpopulations inhabit the fibrotic niche**

183 In rodent models, hepatic endothelial cells are known to regulate fibrogenesis.
184 Clustering of human liver endothelial cells identified seven subpopulations (Fig. 4a).
185 Classical endothelial cell markers did not discriminate between the seven clusters,
186 although Endo(1) was distinct in lacking *CD34* expression (Extended Data Fig. 8a). To
187 fully annotate endothelial subpopulations (Supplementary Note 3, Extended Data Fig.
188 8k), we identified differentially expressed markers (Fig. 4c, Supplementary Table 13),
189 determined functional expression profiles (Extended Data Fig. 8g, Supplementary
190 Table 14), performed transcription factor regulon analysis (Extended Data Fig. 8h,
191 Supplementary Table 15) and assessed spatial distribution via tissue staining (Fig. 4d,
192 Extended Data Fig. 8j).

193 Disease-specific endothelial cells Endo(6) and Endo(7), CD34⁺PLVAP⁺VWA1⁺ and
194 CD34⁺PLVAP⁺ACKR1⁺ respectively (Fig. 4a-c, Extended Data Fig. 8b), expanded in

195 cirrhotic liver tissue (Fig. 4e) and were restricted to the fibrotic niche (Fig. 4d, e,
196 Extended Data Fig. 8c), allowing annotation as scar-associated endothelia SAEndo(1)
197 and SAEndo(2) respectively. In contrast, CD34⁻CLEC4M⁺ Endo(1) (annotated as liver
198 sinusoidal endothelial cells), were reduced in fibrotic livers (Fig. 4b, e). Metagene
199 signature analysis demonstrated that Endo(6) (SAEndo(1)) cells expressed pro-
200 fibrogenic genes including *PDGFD*, *PDGFB*, *LOX*, *LOXL2*; associated ontology terms
201 included extracellular matrix organization (signature A; Extended Data Fig. 8g).
202 Endo(7) (SAEndo(2)) cells displayed an immunomodulatory phenotype (signature B;
203 Extended Data Fig. 8g). The most discriminatory marker for this cluster, *ACKR1*, has
204 a role in regulating leucocyte recruitment²¹. We confirmed increased expression of
205 PLVAP, CD34 and *ACKR1* on endothelial cells isolated from cirrhotic livers
206 (Extended Data Fig. 8d). Flow-based adhesion assays²² demonstrated that cirrhotic
207 endothelial cells display enhanced leucocyte transmigration (Extended Data Fig. 8e),
208 which was attenuated by *ACKR1* knockdown (Extended Data Fig. 8f).

209 **PDGFRA expression defines scar-associated mesenchymal cells**

210 Clustering of human liver mesenchymal cells identified four populations (Fig. 5a, b,
211 Extended Data Fig. 9a, Supplementary Table 16). Cluster Mes(1), distinguished by
212 *MYH11* expression (Fig. 5b, Extended Data Fig. 9a), was identified as vascular smooth
213 muscle cells (VSMC) (Fig. 5c). Mes(4) demonstrated expression of mesothelial
214 markers (Fig. 5b, Extended Data Fig. 9a). Cluster Mes(2) expressed high levels of *RGS5*
215 (Fig. 5b, Extended Data Fig. 9a), and *RGS5* staining identified this population as
216 hepatic stellate cells (HSC) (Fig. 5c). *RGS5*⁺ cells were absent from the fibrotic niche
217 (Fig. 5c). Cluster Mes(3) (distinguished by *PDGFRA* expression) expressed high levels
218 of fibrillar collagens and pro-fibrogenic genes (Fig. 5b, d, Extended Data Fig. 9a).
219 *PDGFRα*⁺ cells expanded in cirrhotic livers (Fig. 5a, e, f) and were mapped to the
220 fibrotic niche (Fig. 5f), enabling annotation as scar-associated mesenchymal cells
221 (SAMES).

222 To study SAMES heterogeneity, further clustering (Extended Data Fig. 9b) identified
223 two populations of SAMES (Extended Data Fig. 9c, d, Supplementary Table 17). *OSRI*
224 expression distinguished cluster SAMESB (Extended Data Fig. 9c), and labelled a
225 subpopulation of periportal cells in healthy liver and scar-associated cells in the fibrotic

226 niche (Extended Data Fig. 9e, f). Cluster SAMesB also expressed other known portal
227 fibroblast markers²³ (Extended Data Fig. 9g).

228 In rodent liver fibrosis models, HSC differentiate into scar-producing myofibroblasts
229 ²⁴⁻²⁶. Pseudotemporal ordering and RNA velocity analyses demonstrated a trajectory
230 from human HSC to SAMes (Extended Data Fig. 9h). Assessment of gene co-
231 expression modules along the HSC-to-SAMes differentiation continuum indicated
232 upregulation of fibrogenic genes including *COL1A1*, *COL1A2*, *COL3A1*, *TIMP1* and
233 downregulation of genes including *RGS5*, *IGFBP5*, *ADAMTS1* and *GEM*, which are
234 known to be downregulated in murine HSC in response to liver injury²⁵ (Extended Data
235 Fig. 9i).

236 **Resolving the multi-lineage interactome in the fibrotic niche**

237 Having defined the scar-associated macrophage, endothelial and mesenchymal
238 populations, we confirmed the close topographical association of these cells within the
239 fibrotic niche (Extended Data Fig. 10a, b), and used CellPhoneDB²⁷ to perform an
240 unbiased ligand-receptor interaction analysis between these populations.

241 Numerous statistically significant paracrine and autocrine interactions were detected
242 between ligands and cognate receptors expressed by SAM Φ , SAEndo and SAMes
243 (Supplementary Table 18, Extended Data Fig. 10f-m). To interrogate how scar-
244 associated NPC regulate fibrosis and to identify tractable therapeutic targets, we
245 focused functional analyses on interactions with SAMes (Fig. 6a, e, Extended Data Fig.
246 10d). In keeping with our data demonstrating that SAM Φ promote fibrillar collagen
247 expression in HSC (Fig. 2g), SAM Φ expressed epidermal growth factor receptor
248 (EGFR) ligands which are known to regulate mesenchymal cell activation²⁸ (Fig. 6a).
249 Additionally, SAM Φ expressed mesenchymal cell mitogens *TNFSF12* and *PDGFB*,
250 signaling to cognate receptors *TNFRSF12A* and *PDGFRA* on SAMes (Fig. 6a). We
251 confirmed localization of these ligand-receptor pairs within the fibrotic niche (Fig. 6b).
252 Both TNFSF12 and PDGF-BB induced primary human HSC proliferation, which was
253 inhibited by blockade of TNFSF12A and PDGFRA respectively (Fig. 6c, d).
254 Conditioned media from primary human SAM Φ promoted primary human HSC

255 proliferation *ex vivo* (Extended Data Fig. 10c), demonstrating a functional role for
256 SAM Φ in regulating SAMes expansion.

257 SAEndo expressed high levels of non-canonical Notch ligands *JAG1*, *JAG2* and *DLL4*
258 interacting with Notch receptor *NOTCH3* on SAMes (Fig. 6e). *NOTCH3* was identified
259 on PDGFR α ⁺ SAMes within the fibrotic niche (Fig. 6f), whilst primary endothelial cells
260 from cirrhotic human liver demonstrated increased expression of *JAG1* (Fig. 6g). Co-
261 culture of primary human HSC and endothelial cells from cirrhotic livers promoted
262 fibrillar collagen production by HSC, which was inhibited by addition of the Notch-
263 signalling inhibitor Dibenazepine (DBZ) (Fig. 6h). Furthermore, knockdown of
264 *NOTCH3* expression in primary human HSC resulted in reduced fibrillar collagen
265 expression (Fig. 6i).

266 In summary, our unbiased dissection of the key ligand-receptor interactions between
267 scar-associated NPC highlights TNFRSF12A, PDGFRA and Notch signaling as
268 important regulators of mesenchymal cell function within the human liver fibrotic
269 niche.

270 **Discussion**

271 Here, using scRNA-seq and spatial mapping, we resolve the fibrotic niche of human
272 liver cirrhosis, identifying pathogenic subpopulations of TREM2⁺CD9⁺ macrophages,
273 ACKR1⁺ and PLVAP⁺ endothelial cells and PDGFR α ⁺ collagen-producing
274 myofibroblasts. We dissect a complex, pro-fibrotic interactome between multiple scar-
275 associated cell lineages and identify highly relevant intra-scar pathways that are
276 potentially druggable. In this era of precision medicine, this unbiased multi-lineage
277 approach should inform the design of highly-targeted combination therapies which will
278 very likely be necessary to achieve effective antifibrotic potency^{3,4}.

279 Application of our novel scar-associated cell markers could also potentially inform
280 molecular pathology-based patient stratification, which is fundamental to the
281 prosecution of successful antifibrotic clinical trials. Our work illustrates the power of
282 single-cell transcriptomics to decode the cellular and molecular basis of human organ
283 fibrosis, providing a conceptual framework for the discovery of relevant therapeutic

284 targets to treat patients with a broad range of fibrotic diseases.

285 **References**

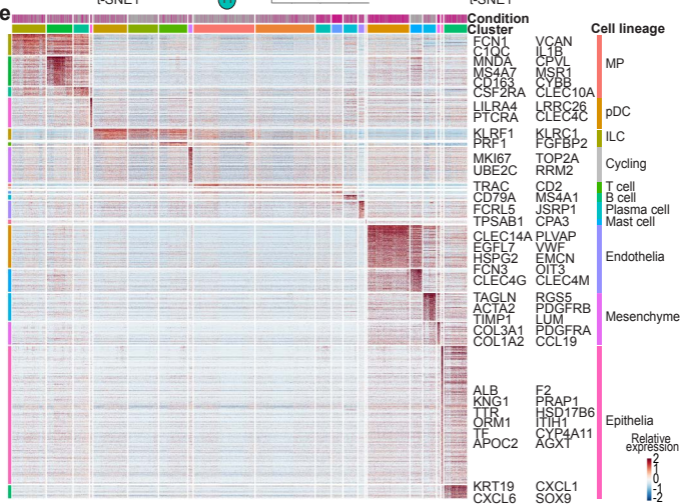
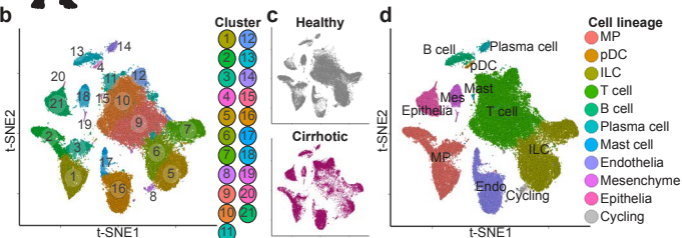
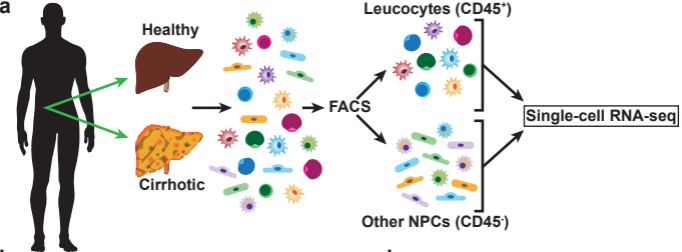
- 286 1. Marcellin, P. & Kutala, B. K. Liver diseases: A major, neglected global public
287 health problem requiring urgent actions and large-scale screening. *Liver Int.*
288 (2018). doi:10.1111/liv.13682
- 289 2. Angulo, P. *et al.* Liver Fibrosis, but No Other Histologic Features, Is
290 Associated With Long-term Outcomes of Patients With Nonalcoholic Fatty
291 Liver Disease. *Gastroenterology* **149**, 389-397.e10 (2015).
- 292 3. Ramachandran, P. & Henderson, N. C. Antifibrotics in chronic liver disease:
293 tractable targets and translational challenges. *Lancet Gastroenterol. Hepatol.* **1**,
294 328–340 (2016).
- 295 4. Friedman, S. L., Neuschwander-Tetri, B. A., Rinella, M. & Sanyal, A. J.
296 Mechanisms of NAFLD development and therapeutic strategies. *Nature*
297 *Medicine* **24**, 908–922 (2018).
- 298 5. Stubbington, M. J. T., Rozenblatt-Rosen, O., Regev, A. & Teichmann, S. A.
299 Single-cell transcriptomics to explore the immune system in health and disease.
300 *Science* **358**, 58–63 (2017).
- 301 6. Duffield, J. S. *et al.* Selective depletion of macrophages reveals distinct,
302 opposing roles during liver injury and repair. *J. Clin. Invest.* **115**, 56–65 (2005).
- 303 7. Ramachandran, P. *et al.* Differential Ly-6C expression identifies the recruited
304 macrophage phenotype, which orchestrates the regression of murine liver
305 fibrosis. *Proc. Natl. Acad. Sci.* **109**, E3186–E3195 (2012).
- 306 8. Karlmark, K. R. *et al.* Hepatic recruitment of the inflammatory Gr1 +
307 monocyte subset upon liver injury promotes hepatic fibrosis. *Hepatology* **50**,
308 261–274 (2009).
- 309 9. Minutti, C. M. *et al.* Local amplifiers of IL-4R α -mediated macrophage
310 activation promote repair in lung and liver. *Science (80-.).* **356**, 1076–1080
311 (2017).
- 312 10. Pradere, J.-P. *et al.* Hepatic macrophages but not dendritic cells contribute to
313 liver fibrosis by promoting the survival of activated hepatic stellate cells in
314 mice. *Hepatology* **58**, 1461–1473 (2013).
- 315 11. Henderson, N. C. *et al.* Galectin-3 regulates myofibroblast activation and
316 hepatic fibrosis. *Proc. Natl. Acad. Sci.* **103**, 5060–5065 (2006).

- 317 12. Seki, E. *et al.* CCR2 promotes hepatic fibrosis in mice. *Hepatology* **50**, 185–
318 197 (2009).
- 319 13. Syn, W. K. *et al.* Osteopontin is induced by hedgehog pathway activation and
320 promotes fibrosis progression in nonalcoholic steatohepatitis. *Hepatology* **53**,
321 106–115 (2011).
- 322 14. Scott, C. L. *et al.* Bone marrow-derived monocytes give rise to self-renewing
323 and fully differentiated Kupffer cells. *Nat. Commun.* **7**, 10321 (2016).
- 324 15. Gomez Perdiguero, E. *et al.* Tissue-resident macrophages originate from yolk-
325 sac-derived erythro-myeloid progenitors. *Nature* **518**, 547–551 (2015).
- 326 16. Mass, E. *et al.* Specification of tissue-resident macrophages during
327 organogenesis. *Science (80-.)*. **353**, (2016).
- 328 17. La Manno, G. *et al.* RNA velocity of single cells. *Nature* **1** (2018).
329 doi:10.1038/s41586-018-0414-6
- 330 18. Butler, A., Hoffman, P., Smibert, P., Papalexi, E. & Satija, R. Integrating
331 single-cell transcriptomic data across different conditions, technologies, and
332 species. *Nat. Biotechnol.* **36**, 411–420 (2018).
- 333 19. Schelker, M. *et al.* Estimation of immune cell content in tumour tissue using
334 single-cell RNA-seq data. *Nat. Commun.* **8**, 2032 (2017).
- 335 20. Ahrens, M. *et al.* DNA Methylation Analysis in Nonalcoholic Fatty Liver
336 Disease Suggests Distinct Disease-Specific and Remodeling Signatures after
337 Bariatric Surgery. *Cell Metab.* **18**, 296–302 (2013).
- 338 21. Pruenster, M. *et al.* The Duffy antigen receptor for chemokines transports
339 chemokines and supports their promigratory activity. *Nat. Immunol.* **10**, 101–8
340 (2009).
- 341 22. Shetty, S., Weston, C. J., Adams, D. H. & Lalor, P. F. A Flow Adhesion Assay
342 to Study Leucocyte Recruitment to Human Hepatic Sinusoidal Endothelium
343 Under Conditions of Shear Stress. *J. Vis. Exp.* (2014). doi:10.3791/51330
- 344 23. Iwaisako, K. *et al.* Origin of myofibroblasts in the fibrotic liver in mice. *Proc.*
345 *Natl. Acad. Sci.* **111**, E3297–E3305 (2014).
- 346 24. Henderson, N. C. *et al.* Targeting of α v integrin identifies a core molecular
347 pathway that regulates fibrosis in several organs. *Nat. Med.* **19**, 1617–1624
348 (2013).

- 349 25. De Minicis, S. *et al.* Gene Expression Profiles During Hepatic Stellate Cell
350 Activation in Culture and In Vivo. *Gastroenterology* **132**, 1937–1946 (2007).
- 351 26. Mederacke, I., Dapito, D. H., Affò, S., Uchinami, H. & Schwabe, R. F. High-
352 yield and high-purity isolation of hepatic stellate cells from normal and fibrotic
353 mouse livers. *Nat. Protoc.* **10**, 305–315 (2015).
- 354 27. Vento-Tormo, R. *et al.* Single-cell reconstruction of the early maternal–fetal
355 interface in humans. *Nature* **563**, 347–353 (2018).
- 356 28. Minutti, C. M. *et al.* A Macrophage-Pericyte Axis Directs Tissue Restoration
357 via Amphiregulin-Induced Transforming Growth Factor Beta Activation.
358 *Immunity* **50**, 645-654.e6 (2019).
- 359
360

361 **Figure 1: Single cell atlas of human liver NPC.**

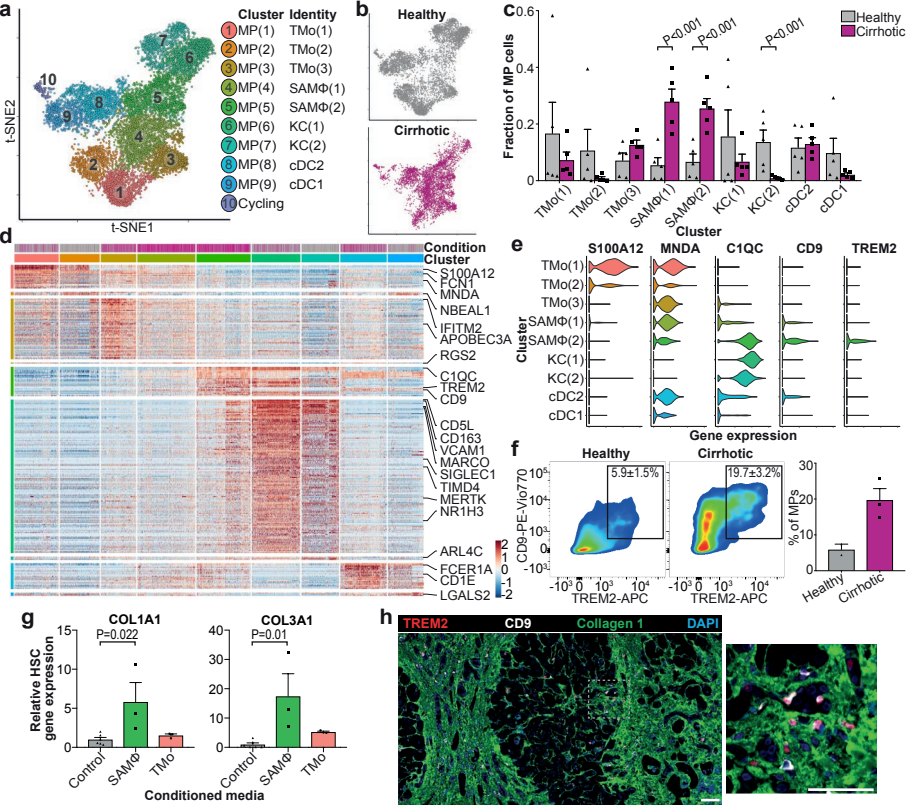
362 **a**, Overview: isolation, FACS-sorting and sc-RNASeq of leucocytes (CD45⁺) and other
363 NPC fractions (CD45⁻). **b**, Clustering 66,135 cells from 5 healthy and 5 cirrhotic human
364 livers. **c**, Annotation by injury condition. **d**, Cell lineage inferred from expression of
365 marker gene signatures. Endo, endothelial cell; ILC, innate lymphoid cell; Mast, mast
366 cell; Mes, mesenchymal cell; MP, mononuclear phagocyte; pDC, plasmacytoid
367 dendritic cell. **e**, Heatmap: cluster marker genes (top, colour coded by cluster and colour
368 coded by condition) and exemplar genes and lineage annotation labelled (right). Cells
369 columns, genes rows.



370 **Figure 2: Identifying scar-associated macrophage subpopulations.**

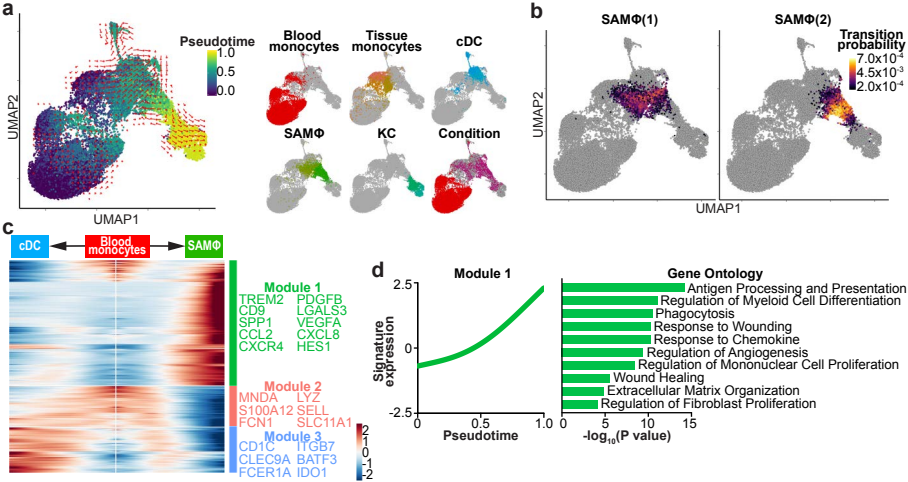
371 **a**, Clustering 10,737 mononuclear phagocytes (MP) from 5 healthy and 5 cirrhotic
372 human livers. TMo, tissue monocyte; SAM Φ , scar-associated macrophage; KC,
373 Kupffer cell; cDC, conventional dendritic cell. **b**, Annotation by injury condition. **c**,
374 Fractions of MP subpopulations in 5 healthy *versus* 5 cirrhotic livers, Mean \pm SEM,
375 Wald test. **d**, Heatmap: MP cluster marker genes (top, colour coded by cluster and
376 condition), exemplar genes labelled (right). Cells columns, genes rows. **e**, Scaled gene
377 expression of SAM Φ and TMo cluster markers across MP cells from healthy (n=5) and
378 cirrhotic (n=5) livers. **f**, Flow cytometry: TREM2⁺CD9⁺ MP fraction in healthy (n=2)
379 *versus* cirrhotic (n=3) liver, Mean \pm SEM. **g**, Primary human hepatic stellate cells (HSC)
380 treated with conditioned media from SAM Φ (n=3) or TMo (n=3); qPCR of stated genes,
381 expression relative to mean expression of control HSC (n=6), Mean \pm SEM, Kruskal-
382 Wallis and Dunn. **h**, Representative immunofluorescence image, cirrhotic liver:
383 TREM2 (red), CD9 (white), collagen 1 (green), DAPI (blue), scale bar 50 μ m.

384



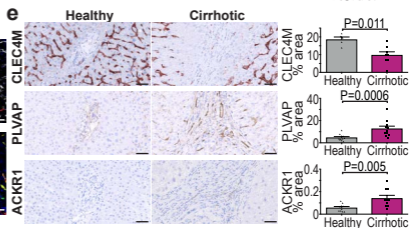
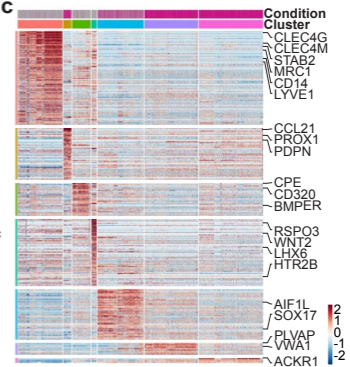
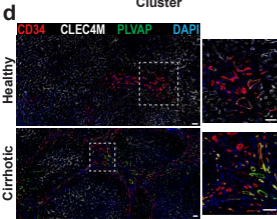
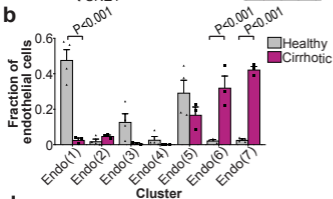
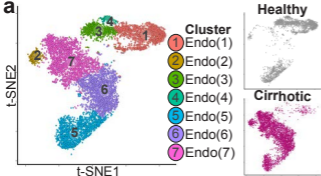
385 **Figure 3: Fibrogenic phenotype of scar-associated macrophages.**

386 **a**, UMAP visualisation, 23,075 cells from liver-resident MP (5 healthy and 5 cirrhotic)
387 and blood monocytes (5 PBMC), annotating *monocle* pseudotemporal dynamics
388 (purple to yellow). RNA velocity field (red arrows) visualised using Gaussian
389 smoothing on regular grid. Right: Annotation of MP subpopulation, injury condition.
390 **b**, Transition probabilities per SAM Φ subpopulation, indicating for each cell the
391 likelihood of transition into either SAM Φ (1) or SAM Φ (2), calculated using RNA
392 velocity (yellow high; purple low; grey below threshold of 2×10^{-4}). **c**, Heatmap: spline
393 curves fitted to genes differentially expressed across blood monocyte-to-SAM Φ (right
394 arrow) and blood monocyte-to-cDC (left arrow) pseudotemporal trajectories, grouped
395 by hierarchical clustering ($k=3$). Gene co-expression modules (colour) labelled right
396 with exemplar genes from each module. **d**, Spline curve fitted to averaged expression
397 of all genes in module 1, along monocyte-to-SAM Φ pseudotemporal trajectory,
398 selected GO enrichment (right), Fisher's exact test.



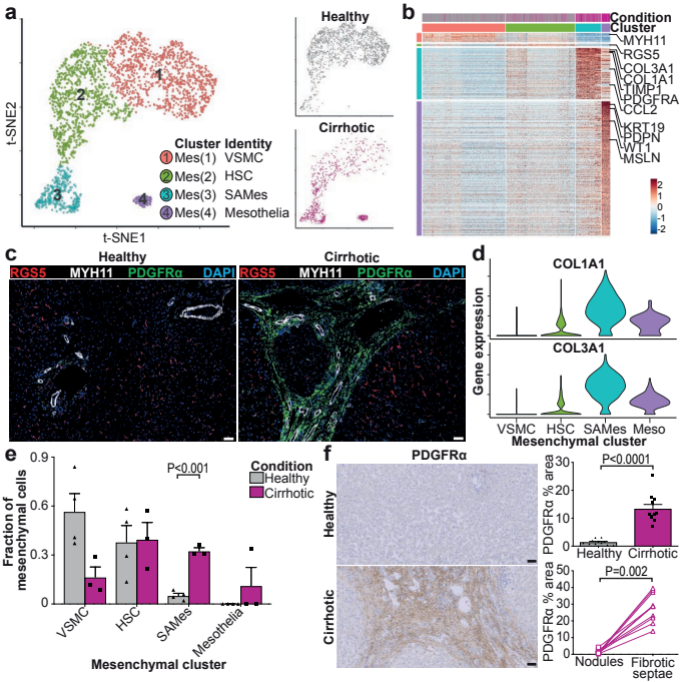
399 **Figure 4: Identifying scar-associated endothelial subpopulations.**

400 **a**, Clustering 8,020 endothelial cells from 4 healthy and 3 cirrhotic human livers,
401 annotating injury condition (right). **b**, Fractions of endothelial subpopulations in
402 healthy (n=4) *versus* cirrhotic (n=3) livers, Mean±SEM, Wald. **c**, Heatmap: endothelial
403 cluster marker genes (colour coded top by cluster and condition), exemplar genes
404 labelled right. Cells columns, genes rows. **d**, Representative immunofluorescence
405 images: CD34 (red), CLEC4M (white), PLVAP (green), DAPI (blue), scale bar 50µm.
406 **e**, Digital pixel quantification: CLEC4M staining healthy (n=5) *versus* cirrhotic liver
407 (n=8), PLVAP staining healthy (n=11) *versus* cirrhotic liver (n=11), ACKR1 staining
408 healthy (n=10) *versus* cirrhotic liver (n=10), scale bars 50µm, Mean±SEM, Mann-
409 Whitney two-tailed.



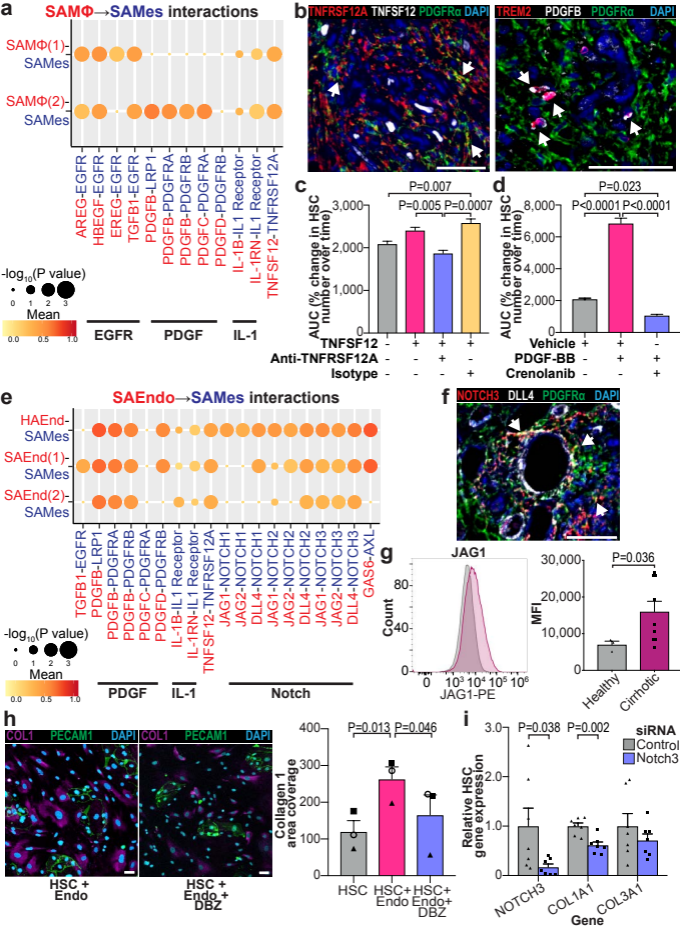
410 **Figure 5: Identifying scar-associated mesenchymal cell populations.**

411 **a**, Clustering 2,318 mesenchymal cells (Mes) from 4 healthy and 3 cirrhotic human
412 livers, annotating injury condition (right). VSMC, vascular smooth muscle cell; HSC,
413 hepatic stellate cell; SAMes, scar-associated mesenchymal cell. **b**, Heatmap:
414 Mesenchymal cluster marker genes (top, colour coded by cluster and condition),
415 exemplar genes labelled (right). Cells columns, genes rows. **c**, Representative
416 immunofluorescence images: RGS5 (red), MYH11 (white), PDGFR α (green), DAPI
417 (blue), scale bars 50 μ m **d**, Scaled gene expression of fibrillar collagens across
418 mesenchymal cells from healthy (n=4) and cirrhotic (n=3) livers. Meso, mesothelial
419 cell. **e**, Fraction of mesenchymal subpopulations in healthy (n=4) *versus* cirrhotic (n=3)
420 livers, Mean \pm SEM, Wald test. **f**, PDGFR α immunohistochemistry, digital pixel
421 quantification of healthy (n=11) *versus* cirrhotic (n=11) liver (top right), Mean \pm SEM,
422 Mann-Whitney two-tailed. PDGFR α pixel quantification in fibrotic septae and
423 parenchymal nodules in 10 cirrhotic livers (bottom right), Wilcoxon two-tailed, scale
424 bars 50 μ m.



425 **Figure 6: Multi-lineage interactions in the fibrotic niche.**

426 **a**, Dotplot: ligand-receptor interactions between SAM Φ (n=10 human livers) and
427 SAMes (n=7 human livers). X-axis, ligand (red) and cognate receptor (blue); y-axis,
428 cell populations expressing ligand (red) and receptor (blue); circle size, P value
429 (permutation test); colour (red, high; yellow, low), means of average ligand and
430 receptor expression levels in interacting subpopulations. **b**, Representative
431 immunofluorescence images, fibrotic niche. Left, TREM2 (red), PDGFB (white),
432 PDGFR α (green), DAPI (blue), arrows TREM2⁺PDGFB⁺ cells. Right, TNFRSF12A
433 (red), TNFSF12 (white), PDGFR α (green), DAPI (blue), arrows
434 TNFRSF12A⁺PDGFR α ⁺ cells, scale bars 50 μ m. **c to d**, HSC proliferation assay: y-
435 axis, area under curve (AUC) of % change in HSC number over time (hours),
436 Mean \pm SEM, one-way ANOVA and Tukey. **c**, Control, TNFSF12, anti-TNFRSF12A,
437 isotype control, all n=3. **d**, Vehicle, PDGF-BB, Crenolanib, all n=3. **e**, Dotplot: ligand-
438 receptor interactions between SAEndo (n=7 human livers) and SAMes (n=7 human
439 livers). X-axis, ligand (red) and cognate receptor (blue); y-axis, cell populations
440 expressing ligand (red) and receptor (blue); circle size, P value (permutation test);
441 colour (red, high; yellow, low), means of average ligand and receptor expression levels
442 in interacting subpopulations. **f**, Representative immunofluorescence image, fibrotic
443 niche. NOTCH3 (red), DLL4 (white), PDGFR α (green), DAPI (blue), arrows
444 NOTCH3⁺PDGFR α ⁺ cells, scale bar 50 μ m. **g**, Endothelial cell JAG1 flow cytometry:
445 healthy (n=3) or cirrhotic (n=9) liver, representative histogram (left), mean
446 fluorescence intensity (MFI, right), Mean \pm SEM, Mann-Whitney two-tailed. **h**,
447 Cirrhotic endothelial cell and HSC co-culture, Notch inhibitor Dibenazepine (DBZ).
448 Representative immunofluorescence images (left), Collagen 1 (magenta), PECAM1
449 (green), DAPI (blue). Digital pixel analysis (right); collagen 1 area, n=3, Mean \pm SEM,
450 RM one-way ANOVA and Tukey. **n**, HSC gene knockdown: control (n=7) or *NOTCH3*
451 (n=7) siRNA, qPCR of stated gene, expression relative to mean expression of control
452 siRNA, Mean \pm SEM, Mann-Whitney two-tailed.



453 **Methods**

454 **Study subjects**

455 Local approval for procuring human liver tissue and blood samples for scRNA-seq,
456 flow cytometry and histological analysis was obtained from the NRS BioResource and
457 Tissue Governance Unit (Study Number SR574), following review at the East of
458 Scotland Research Ethics Service (Reference 15/ES/0094). All subjects provided
459 written informed consent. Healthy background non-lesional liver tissue was obtained
460 intraoperatively from patients undergoing surgical liver resection for solitary colorectal
461 metastasis at the Hepatobiliary and Pancreatic Unit, Department of Clinical Surgery,
462 Royal Infirmary of Edinburgh. Patients with a known history of chronic liver disease,
463 abnormal liver function tests or those who had received systemic chemotherapy within
464 the last four months were excluded from this cohort. Cirrhotic liver tissue was obtained
465 intraoperatively from patients undergoing orthotopic liver transplantation at the
466 Scottish Liver Transplant Unit, Royal Infirmary of Edinburgh. Blood from patients with
467 a confirmed diagnosis of liver cirrhosis were obtained from patients attending the
468 Scottish Liver Transplant Unit, Royal Infirmary of Edinburgh. Patients with liver
469 cirrhosis due to viral hepatitis were excluded from the study. Patient demographics are
470 summarised in Extended Data Fig. 1a. Isolation of primary hepatic macrophage
471 subpopulations and endothelial cells from healthy and cirrhotic livers for cell culture
472 and analysis of secreted mediators was performed at the University of Birmingham,
473 UK. Local ethical approval was obtained (Reference 06/Q2708/11, 06/Q2702/61) and
474 all patients provided written, informed consent. Liver tissue was acquired from
475 explanted diseased livers from patients undergoing orthotopic liver transplantation,
476 resected liver specimens or donor livers rejected for transplant at the Queen Elizabeth
477 Hospital, Birmingham. For histological assessment of NAFLD biopsies, anonymised
478 unstained formalin-fixed paraffin-embedded liver biopsy sections encompassing the
479 complete NAFLD spectrum were provided by the Lothian NRS Human Annotated
480 Bioresource under authority from the East of Scotland Research Ethics Service REC 1,
481 reference 15/ES/0094.

482 **Human tissue processing**

483 Importantly, to minimise artefacts²⁹, we developed a rapid tissue processing pipeline,
484 obtaining fresh non-ischaemic liver tissue taken by wedge biopsy prior to the
485 interruption of the hepatic vascular inflow during liver surgery or transplantation, and
486 immediately processing this for FACS. This enabled a workflow time of under three
487 hours from patient to single-cell droplet encapsulation.

488 For human liver scRNA-seq and flow cytometry analysis, a wedge biopsy of non-
489 ischaemic fresh liver tissue (2-3 grams) was obtained by the operating surgeon, prior to
490 interruption of the hepatic vascular inflow. This was immediately placed in HBSS
491 (Gibco) on ice. The tissue was then transported directly to the laboratory and
492 dissociation routinely commenced within 20 minutes of the liver biopsy. To enable
493 paired histological assessment, a segment of each liver specimen was also fixed in 4%
494 neutral-buffered formalin for 24 hours followed by paraffin-embedding. Additional
495 liver samples, obtained via the same method, were fixed in an identical manner and
496 used for further histological analysis. For human macrophage cell sorting and
497 endothelial cell isolation, liver tissue (40 grams) was used from cirrhotic patients
498 undergoing orthotopic liver transplantation or control samples from donor liver or liver
499 resection specimens.

500 **Animals**

501 Adult male C57BL/6JCrI mice aged 8-10 weeks were purchased from Charles River.
502 Mice were housed under specific pathogen-free conditions at the University of
503 Edinburgh. All experimental protocols were approved by the University of Edinburgh
504 Animal Welfare and Ethics Board in accordance with UK Home Office regulations.
505 Liver fibrosis was induced with 4 weeks (9 injections) of twice-weekly intraperitoneal
506 carbon tetrachloride (CCl₄) at a dose of 0.4 µl/g body weight, diluted 1:3 in olive oil as
507 previously described⁷. Mice were randomly assigned to receive CCl₄ or to serve as
508 healthy controls. No sample size calculation or blinding was performed. Liver tissue
509 was harvested 24 hours following the final CCl₄ injection, a time of active fibrogenesis⁷.
510 Comparison was made to age-matched uninjured mice.

511 **Preparation of single-cell suspensions**

512 For human liver scRNA-seq, liver tissue was minced with scissors and digested in
513 5mg/ml pronase (Sigma-Aldrich, P5147-5G), 2.93mg/ml collagenase B (Roche,
514 11088815001) and 1.9mg/ml DNase (Roche, 10104159001) at 37°C for 30 minutes
515 with agitation (200–250 r.p.m.), then strained through a 120µm nybolt mesh along with
516 PEB buffer (PBS, 0.1% BSA, and 2mM EDTA) including DNase (0.02mg/ml).
517 Thereafter all processing was done at 4°C. The cell suspension was centrifuged at 400g
518 for 7 minutes, supernatant removed, cell pellet resuspended in PEB buffer and DNase
519 added (0.02mg/ml), followed by additional centrifugation (400g, 7 minutes). Red blood
520 cell lysis was performed (BioLegend, 420301), followed by centrifugation (400g, 7
521 minutes), resuspension in PEB buffer and straining through a 35µm filter. Following
522 another centrifugation at 400g for 7 minutes, cells were blocked in 10% human serum
523 (Sigma-Aldrich, H4522) for 10 minutes at 4°C prior to antibody staining.

524 For both human liver macrophage flow cytometry analysis and cell sorting and mouse
525 liver macrophage flow cytometry, cell sorting and scRNA-seq, single-cell suspensions
526 were prepared as previously described, with minor modifications³⁰. In brief, liver tissue
527 was minced and digested in an enzyme cocktail 0.625 mg/ml collagenase D (Roche,
528 11088882001), 0.85 mg/ml collagenase V (Sigma-Aldrich, C9263-1G), 1 mg/ml
529 dispase (Gibco, Invitrogen, 17105-041), and 30 U/ml DNase (Roche, 10104159001) in
530 RPMI-1640 at 37°C for 20 minutes (mouse) or 45 minutes (human) with agitation
531 (200–250 r.p.m.), before being passed through a 100µm filter. Following red blood cell
532 lysis (BioLegend, 420301), cells were washed in PEB buffer and passed through a
533 35µm filter. Before the addition of antibodies, cells from human samples were blocked
534 in 10% human serum (Sigma-Aldrich, H4522) and mouse samples were blocked in
535 anti-mouse CD16/32 antibody (1:100; Biolegend, 101302) and 10% normal mouse
536 serum (Sigma, M5905) for 10 minutes at 4 °C.

537 For human PBMC scRNA-seq, 4.9ml peripheral venous blood samples were collected
538 in EDTA-coated tubes (Sarstedt, S-Monovette® 4.9ml K3E) and placed on ice. Blood
539 samples were transferred into a 50ml Falcon tube. Following red cell lysis (Biolegend,
540 420301), blood samples were then centrifuged at 500g for 5 minutes and supernatant
541 was removed. Pelleted samples were then resuspended in staining buffer (PBS plus 2%
542 BSA; Sigma-Aldrich) and centrifugation was repeated. Samples were then blocked in

543 10% human serum (Sigma-Aldrich, H4522) in staining buffer on ice for 30 minutes.
544 Cells were then resuspended in staining buffer and passed through a 35µm filter prior
545 to antibody staining.

546 **Flow cytometry and cell sorting**

547 Incubation with primary antibodies was performed for 20 minutes at 4°C. All
548 antibodies, conjugates, lot numbers and dilutions used in this study are presented in
549 Supplementary Table 19. Following antibody staining, cells were washed with PEB
550 buffer. For both human macrophage flow cytometry analysis and cell sorting, cells were
551 then incubated with streptavidin-BV711 for 20 minutes at 4°C (Biolegend 405241;
552 Dilution 1:200). For human and mouse cell sorting (FACS) and mouse flow cytometry
553 analysis, cell viability staining (DAPI; 1:1000 dilution) was then performed,
554 immediately prior to acquiring the samples.

555 Human cell sorting for scRNA-seq was performed on a BD Influx (Becton Dickinson,
556 Basel, Switzerland). Viable single CD45⁺ (leucocytes) or CD45⁻ (other non-
557 parenchymal cells) cells were sorted from human liver tissue (Extended Data Fig. 1b)
558 and viable CD45⁺ CD66b⁻ (PBMC) cells were sorted from peripheral blood (Extended
559 Data Fig. 1c) and processed for droplet-based scRNA-seq.

560 To generate conditioned media from cirrhotic liver macrophage subpopulations, cells
561 were sorted on a BD FACSAriaTM Fusion (Becton Dickinson, Basel, Switzerland).
562 Sorted SAMΦ (viable CD45⁺Lin⁻HLA-DR⁺CD14⁺CD16⁺CD163⁻TREM2⁺CD9⁺),
563 TMo (viable CD45⁺Lin⁻HLA-DR⁺CD14⁺CD16⁺CD163⁻TREM2⁻CD9⁻) and KC (viable
564 CD45⁺Lin⁻HLA-DR⁺CD14⁺CD16⁺CD163⁺CD9⁻) were plated in 12-well plates
565 (Corning, 3513) in DMEM (Gibco, 41965039) containing 2% FBS (Gibco, 10500056)
566 at 1x10⁶ cells/ml for 24 hours at 37°C 5%CO₂. Control wells contained media alone.
567 Conditioned media was collected, centrifuged at 400g for 10 minutes and supernatant
568 stored at -80°C.

569 For human macrophage flow cytometry analysis, following surface antibody staining,
570 cells were stained with Zombie NIR fixable viability dye (Biolegend, 423105)
571 according to manufacturers' instructions. Cells were washed in PEB then fixed in IC

572 fixation buffer (Thermo-Fisher, 00-8222-49) for 20 minutes at 4°C. Fixed samples were
573 stored in PEB at 4°C until acquisition. Flow cytometry acquisition was performed on
574 6-laser Fortessa flow cytometer (Becton Dickinson, Basel, Switzerland). The gating
575 strategy is shown (Extended Data Fig. 4f, Fig. 2f).

576 Mouse macrophage cell sorting for scRNA-seq and co-culture experiments was
577 performed on a BD FACSAriaII (Becton Dickinson, Basel, Switzerland). For scRNA-
578 seq, viable CD45⁺ Lin(CD3, NK1.1, Ly6G, CD19)⁻ cells were sorted from healthy
579 (n=3) and CCl₄-treated (n=3) mice and processed for droplet-based scRNA-seq. For
580 transwell co-culture, viable CD45⁺ Lin⁻ CD11b⁺ F4/80⁺ TIMD4⁻ CD9⁺ (mSAMΦ) or
581 CD9⁻ (mTMO) cells were sorted from CCl₄-treated mice (Extended Data Fig. 6e). Flow
582 cytometry analysis on macrophages from healthy and CCl₄-treated mice was also
583 performed on a BD FACSAriaII (Becton Dickinson, Basel, Switzerland), using the
584 same gating strategy (Extended Data Fig. 6e). All flow cytometry data was analysed
585 using Flowjo software (Treestar, Ashland, TN).

586 **Luminex Assay**

587 Detection of CCL2, Galectin-3, IL-1β, CXCL8 and Osteopontin (SPP1) and CD163
588 proteins in conditioned media from human liver macrophage subpopulations was
589 performed using a custom human luminex assay (R&D systems), according to the
590 manufacturers protocol. Data was acquired using a Bio-Plex[®] 200 (Bio-Rad, UK) and
591 is presented a median fluorescence intensity (MFI) for each analyte.

592 **Cell Culture**

593 *Human hepatic stellate cell activation*

594 Primary human hepatic stellate cells (HSC) were purchased (ScienCell, 5300) and
595 cultured in stellate cell medium (SteCM, ScienCell, 5301) on Poly-L-Lysine (Sigma,
596 P4832) coated T75 tissue culture flasks, according to the suppliers protocol. All
597 experiments were performed using cells between passage 3 and 5. For assessment of
598 fibrillar collagen gene expression, HSC were plated at 75,000 cells per well in 24 well-
599 plates (Costar, 3524) in HSC media consisting of DMEM (Gibco, 21969-035)
600 supplemented with 20 μM HEPES (Sigma, H3375), 2 mM L-Glutamine (Gibco ,

601 25030-024), 1% Penicillin Streptomycin (Gibco, 15140-122, Gibco) and 2% Foetal
602 Bovine Serum (FBS, Gibco, 10270). HSC were serum starved overnight (in HSC media
603 without FBS), washed with PBS, then 250µl of conditioned media from primary human
604 macrophage subpopulations added for 24 hours. HSC were harvested for RNA.

605 *Human hepatic stellate cell proliferation*

606 For proliferation assays, following serum starvation HSC were harvested using TrypLE
607 Express (Gibco, Cat. no. 12604013), re-suspended in HSC media at 2.5×10^4 /ml with
608 Incucyte NucLight Rapid Red (Essen Biosciences, 4717) at a dilution of 1 in 500 and
609 seeded into 384-well plates (Greiner Bio-One, 781090) at 25µl per well. HSC were then
610 treated with control media or (i) PDGF-BB (10ng/ml; Peprotech, 100-14B) or
611 TNFSF12 (100ng/ml; Peprotech, 310-06-5) with or without the PDGFR α inhibitor
612 Crenolanib³¹ (1µM; Cayman chemicals, CAY1873), anti-TNRSF12A (2µg/ml; Life
613 Technologies, 16-9018-82, clone ITEM-4), mouse IgG2b kappa isotype control
614 antibody (2µg/ml; Life Technologies, 16-4732-82, clone eBMG2b) or vehicle control
615 as indicated or (ii) conditioned media from human hepatic macrophage subpopulations
616 as indicated. The final volume was 50µl for all conditions. Cells were then incubated
617 in an Incucyte ZOOM live cell analysis system (Essen Biosciences) humidified at 37°C
618 with 5% CO₂ with imaging every 3 hours using the 10x optic for either 87 hours
619 (recombinant cytokines/inhibitors) or 39 hours (macrophage conditioned media).
620 Analysis was performed with the Incucyte proprietary analysis software (version
621 2018A) by using machine learning to distinguish the individual nuclei (stained red by
622 the NucLight Rapid Red dye) and perform nuclear counts of the images at each 3 hour
623 time point over the period of culture. Data are expressed as area under curve (AUC)
624 for % change in nuclear number from baseline *versus* time (hours), calculated in
625 GraphPad Prism (GraphPad Software, USA).

626 *Gene knockdown in human hepatic stellate cells*

627 Knockdown of NOTCH3 in human HSC was performed using siRNA. HSC were plated
628 at 75,000 cells per well in a 12 well plate (Costar, 3513) followed by serum starvation
629 overnight (in HSC medium without FBS). siRNA duplexes with Lipofectamine
630 RNAiMAX Transfection Reagent (ThermoFisher, 13778075) were prepared in
631 OptiMEM (ThermoFisher, 31985070) according to the manufacturer's

632 recommendations, and used at a concentration of 50nM. Cells were exposed to the
633 duplex for 48 hours, in HSC media containing 2% FBS. Cells were harvested for RNA
634 and RT-qPCR. Knockdown efficiency was assessed by NOTCH3 RT-qPCR. The best
635 siRNA for knockdown was determined empirically using the FlexiTube GeneSolution
636 kit (Qiagen, GS4854). HSC treated with control siRNA (Qiagen, 1027280) and siRNA
637 for NOTCH3 (Qiagen, Hs_NOTCH3_3, SI00009513; knockdown 83%) were then
638 assessed for fibrillar collagen gene expression.

639 *Mouse hepatic stellate cell activation*

640 Primary murine HSC culture were isolated from healthy mice as described²⁶. Briefly,
641 after cannulation of the inferior vena cava, the portal vein was cut to allow retrograde
642 step-wise perfusion with pronase (Sigma, P5147) and collagenase D (Roche,
643 11088882001) containing solutions, before *ex vivo* digestion in a solution containing
644 pronase, collagenase D and Dnase1 (Roche, 10104159001). HSC were isolated from
645 the digest solution by Histodenz (Sigma, D2158-100G) gradient centrifugation. HSC
646 were plated at a density of 400,000 cells per well in a 24 well plate (Costar, 3524) in
647 HSC media containing 10% FBS. Following overnight culture, cells were washed with
648 PBS and cultured in HSC media containing 2% FBS. For macrophage co-culture,
649 transwell inserts (0.4µm polyester membrane; Costar, 3470) were then placed above
650 adherent HSC. FACS-sorted CD9⁺ mSAMΦ or CD9⁻ mTMO from CCl₄-treated mice
651 were resuspended in HSC media containing 2% FBS at 400,000 cells/ml and 200,000
652 cells added to the top of the transwell insert. Co-culture proceeded for 48 hours and
653 HSC were harvested for RNA. Quiescent HSC (harvested at start of co-culture) were
654 used as a control population.

655 *Human liver endothelial cell isolation*

656 Human liver endothelial cells (LEC) were isolated from cirrhotic explant livers and
657 non-fibrotic control donor liver as previously described³². Endothelial cells were
658 cultured on plasticware coated with rat-tail collagen (Sigma, C3867) in complete LEC
659 medium consisting of endothelial basal media (ThermoFisher, 11111044) containing
660 10% heat inactivated human serum (tcsBiosciences, CS100-500), 100U penicillin, 100
661 µg/mL streptomycin, 2mM glutamine (Sigma, G6784), VEGF (10 ng/mL; Peprotech,

662 100-20) and 10 ng/mL HGF (10 ng/mL; Peprotech, 100-39). LEC expression of
663 PLVAP, CD34, ACKR1 and JAG1 was assessed using flow cytometry.

664 *Flow-based adhesion assays*

665 Flow-based adhesion assays were performed as described^{22,32}. Briefly, LEC from
666 healthy and cirrhotic liver were seeded into a rat-tail collagen coated Ibidi slide VI^{0.4}
667 (Ibidi, 80606) at a density to give a monolayer and incubated overnight. Peripheral
668 blood was collected from healthy donors in EDTA-coated tubes. Peripheral blood
669 monocuclear cells (PBMC) were isolated using a lympholyte density gradient
670 (Cedarlane laboratories) then washed in PBS containing 1mM Ca²⁺, 0.5 mM Mg²⁺ and
671 0.15% bovine serum albumin (PBS/BSA). Monocytes were enriched from PBMC using
672 pan-monocyte isolation kit (Miltenyi biotech, 130-096-537) according to the
673 manufacturer's protocol. For flow-based adhesion assay, cells were resuspended at 10⁶
674 cells per millilitre in endothelial basal media (ThermoFisher, 11111044) containing
675 0.15% BSA, then perfused over the LEC monolayer for 5min at 0.28ml/min. Non-
676 adherent cells were washed off during 5min perfusion of 0.15% BSA human basal
677 endothelial medium and 10 random non-overlapping images were randomly recorded
678 from each channel. Total adherent (bright-phase; expressed as cell number/mm²/1
679 million cells perfused) and transmigrating cells (dark-phase; expressed as percentage
680 total adherent cells) on an LEC monolayer from each patient were counted and
681 quantified as previously described²².

682 *Gene knockdown in endothelial cells*

683 Knockdown of ACKR1 and PLVAP gene expression in human cirrhotic LEC was
684 performed using siRNA as previously described³². In brief, siRNA duplexes for
685 PLVAP, ACKR1, or negative control (Qiagen, 1027280) with Lipofectamine
686 RNAiMAX Transfection Reagent (ThermoFisher, 13778075) were prepared in
687 OptiMEM (ThermoFisher, 31985070) according to the manufacturer's
688 recommendations, and used at a concentration of 25nM. Cells were exposed to the
689 duplex for 4 hours at 37°C after which time the media was replaced with endothelial
690 basal media containing 10% heat-inactivated human serum for 24 hours. The media
691 was then replaced with complete LEC media and incubated at 37°C with 5% CO₂ for a
692 further 24 hours. Knockdown efficacy was assessed by flow cytometry and mean

693 fluorescence intensity (Extended Data Fig. 8f). The best siRNA for knockdown was
694 determined empirically using the FlexiTube GeneSolution kit (Qiagen, GS83483
695 (PLVAP) and GS2532 (ACKR1)). For flow-based adhesion assays, siRNAs for
696 PLVAP (Qiagen, Hs_PLVAP_1, SI00687547; knockdown 50.6%), ACKR1 (Qiagen,
697 Hs_Fy_5, SI02627667; knockdown 37.7%) or control siRNA were selected. 90,000
698 LEC from cirrhotic patients (n=6) were seeded into channels of a rat-tail collagen
699 coated Ibidi slide VI^{0.4}, gene knockdown performed, followed by flow-based adhesion
700 assay as described above.

701 *Endothelial and hepatic stellate cell co-culture*

702 HSC (15,000 cells) were seeded into an Ibidi slide VI^{0.4} with and without primary
703 human LEC (15,000 cells) from individual cirrhotic patients (n=3) in LEC complete
704 medium. After 2h, all growth factor supplements were removed and cells were cultured
705 for a further 72 hours in endothelial basal media containing 10% heat-inactivated
706 human serum ± Notch-signalling inhibitor Dibenzazepine (10µM, Bio-Techne,
707 4489/10) or vehicle (DMSO) control. Cells were fixed in 4% PFA for 30 minutes,
708 permeabilised with 0.3% Triton PBS for 5 minutes, blocked with 10% goat serum in
709 PBS for 30 minutes followed by primary antibody incubation (mouse anti-PECAM1
710 and rabbit anti-collagen 1; see Supplementary Table 19) for 1 hour. Cells were washed
711 in 0.1% Triton PBS followed by addition of fluorescently-conjugated secondary
712 antibodies (1:500 dilution) for 1 hour. Cells were mounted with Pro-long Gold anti-
713 fade DAPI, images were taken on the Confocal Microscope Zeiss LSM780, and
714 collagen 1 area staining quantified using IMARIS.

715 **RNA extraction and RT-qPCR**

716 RNA was isolated from HSC using the RNeasy Plus Micro Kit (Qiagen, 74034) and
717 cDNA synthesis performed using QuantiTect Reverse Transcription Kit (Qiagen,
718 205313) according to the manufacturers' protocol. Reactions were performed in
719 triplicate in 384-well plate format and were assembled using the QIAgility automated
720 pipetting system (Qiagen). RT-qPCR for human HSC was performed using PowerUp
721 SYBR Green Master Mix (ThermoFisher, A25777) with the following primers (all
722 Qiagen): *GAPDH* (QT00079247), *COL1A1* (QT00037793), *COL3A1* (QT00058233),

723 *NOTCH3* (QT00003374). RT-qPCR for mouse HSC was performed using TaqMan
724 Fast Advanced Master Mix (ThermoFisher, 4444557) with the following primers:
725 *Gapdh* (ThermoFisher, Mm9999915_g1) and *Col3a1* (ThermoFisher,
726 Mm00802300_m1). Samples were amplified on an ABI 7900HT FAST PCR system
727 (Applied Biosystems, ThermoFisher Scientific). Data was analysed using
728 ThermoFisher Connect cloud qPCR analysis software (ThermoFisher Scientific). The
729 $2^{-\Delta\Delta Ct}$ quantification method, using *GAPDH* for normalization, was used to estimate
730 the amount of target mRNA in samples, and expression calculated relative to average
731 mRNA expression levels from control samples.

732 **Immunohistochemistry, immunofluorescence, smFISH**

733 Formalin-fixed paraffin-embedded human liver tissue was cut into 4 μm sections,
734 dewaxed, rehydrated, then incubated in 4% neutral-buffered formalin for 20 minutes.
735 Following heat-mediated antigen retrieval in pH6 sodium citrate (microwave; 15
736 minutes), slides were washed in PBS and incubated in 4% hydrogen peroxide for 10
737 minutes. Slides were then washed in PBS, blocked using protein block (GeneTex,
738 GTX30963) for 1 hour at room temperature before incubation with primary antibodies
739 for 1 hour at room temperature. A full list of primary antibodies and conditions are
740 shown in Supplementary Table 19. Slides were washed in PBST (PBS plus 0.1%
741 Tween20; Sigma-Aldrich, P1379) then incubated with ImmPress HRP Polymer
742 Detection Reagents (depending on species of primary; rabbit, MP-7401; mouse, MP-
743 6402-15; goat, MP-7405; all Vector Laboratories) for 30 minutes at room temperature.
744 Slides were washed in PBS followed by detection. For DAB staining, sections were
745 incubated with DAB (DAKO, K3468) for 5 minutes and washed in PBS before a
746 haematoxylin (Vector Laboratories, H3404) counterstain. For multiplex
747 immunofluorescence staining, following the incubation with ImmPress and PBS wash,
748 initial staining was detected using either Cy3, Cy5, or Fluorescein tyramide (Perkin-
749 Elmer, NEL741B001KT) at a 1:1000 dilution. Slides were then washed in PBST
750 followed by further heat treatment with pH6 sodium citrate (15 minutes), washes in
751 PBS, protein block, incubation with the second primary antibody (incubated overnight
752 at 4°C), ImmPress Polymer and tyramide as before. This sequence was repeated for the

753 third primary antibody (incubated at room temperature for 1 hour) and a DAPI-
754 containing mountant was then applied (ThermoFisher Scientific, P36931).

755 For AMEC Staining (only CLEC4M immunohistochemistry), all washes were carried
756 out with TBST (dH₂O, 200mM Tris, 1.5M NaCl, 1% Tween20 (all Sigma-Aldrich)
757 pH7.5) and peroxidase blocking was carried out for 30mins in 0.6% hydrogen peroxide
758 in Methanol. Sections were incubated with AMEC (Vector Laboratories, SK-4285) for
759 20 minutes and washed in TBST (dH₂O, 200mM Tris, 1.5M NaCl, 1% Tween20 (all
760 Sigma-Aldrich)) before a haematoxylin (Vector Laboratories, SK-4285) counterstain.

761 For combined single-molecule fluorescent in situ hybridization (smFISH) and
762 immunofluorescence, detection of TREM2 was performed using the RNAscope[®] 2.5
763 LS Reagent Kit - BrownAssay (Advanced Cell Diagnostics (ACD)) in accordance with
764 the manufacturer's instructions. Briefly, 5 µm tissue sections were dewaxed, incubated
765 with endogenous enzyme block, boiled in pretreatment buffer and treated with protease,
766 followed by target probe hybridization using the RNAscope[®] LS 2.5 Hs-TREM2
767 (420498, ACD) probe. Target RNA was then detected with Cy3 tyramide (Perkin-
768 Elmer, NEL744B001KT) at 1:1000 dilution. The sections were then processed through
769 a pH6 sodium citrate heat-mediated antigen retrieval, hydrogen peroxidase treatment
770 and protein block (all as for multiplex immunofluorescence staining as above). MNDA
771 antibody was applied overnight at 4°C, completed using a secondary ImmPress HRP
772 Anti-Rabbit Peroxidase IgG (Vector Laboratories, MP7401), visualised using a
773 Flourescein tyramide (Perkin-Elmer, NEL741B001KT) at a 1:1000 dilution and stained
774 with DAPI.

775 Brightfield and fluorescently-stained sections were imaged using the slide scanner
776 AxioScan.Z1 (Zeiss) at 20X magnification (40X magnification for smFISH). Images
777 were processed and scale bars added using Zen Blue (Zeiss) and Fiji software³³.

778 **Cell counting and image analysis**

779 Automated cell counting was performed using QuPath software³⁴. Briefly, DAB-
780 stained whole tissue section slide-scanned images (CZI files) were imported into
781 QuPath. Cell counts were carried out using the positive cell detection tool, detecting

782 haematoxylin-stained nuclei and then thresholding for positively-stained DAB cells,
783 generating DAB-positive cell counts/mm² tissue. Identical settings and thresholds were
784 applied to all slides for a given stain and experiment. For cell counts of fibrotic septae
785 vs parenchymal nodules, the QuPath segmentation tool was used to segment the DAB-
786 stained whole tissue section into fibrotic septae or non-fibrotic parenchymal nodule
787 regions using tissue morphological characteristics (Fig. 2j). Positive cell detection was
788 then applied to the fibrotic and non-fibrotic regions in turn, providing cell DAB-positive
789 cell counts/mm² in fibrotic septae and non-fibrotic parenchymal nodules for each tissue
790 section.

791 Digital morphometric pixel analysis was performed using the Trainable Weka
792 Segmentation (TWS) plugin³⁵ in Fiji software³³. Briefly, each stained whole tissue
793 section slide-scanned image was converted into multiple TIFF files in Zen Blue
794 software (Zeiss). TIFF files were imported into Fiji and TWS plugin trained to produce
795 a classifier which segments images into areas of positive staining, tissue background
796 and white space³⁵. The same trained classifier was then applied to all TIFF images from
797 every tissue section for a particular stain, providing a percentage area of positive
798 staining for each tissue section. For digital morphometric quantification of positive
799 staining of fibrotic septae *versus* parenchymal nodules, TIFF images were segmented
800 into fibrotic septae or non-fibrotic parenchymal nodule regions using tissue
801 morphological characteristics, followed by analysis using the TWS plugin in Fiji
802 software.

803 **Histological assessment of NASH sections**

804 Haematoxylin and eosin and picro-sirius red stained sections from each case were
805 whole-slide imaged using a NanoZoomer imager (Hamamatsu Photonics, Japan).
806 Images of stained sections were independently scored by a consultant liver transplant
807 histopathologist (T.J.K.) at the national liver transplant centre with experience in trial
808 scoring by applying the ordinal NAFLD activity score³⁶. For observer-independent
809 quantification of picro-sirius red positive staining, images were split using ndpisplit³⁷
810 into tiles of x5 magnification before the application of a classifier that had been trained

811 by the liver histopathologist using the machine learning WEKA plugin in FIJI^{33,35}, as
812 previously described³⁸. All analysis was undertaken blind to all other data.

813 **Droplet-based scRNA-seq**

814 Single cells were processed through the Chromium™ Single Cell Platform using the
815 Chromium™ Single Cell 3' Library and Gel Bead Kit v2 (10X Genomics, PN-120237)
816 and the Chromium™ Single Cell A Chip Kit (10X Genomics, PN-120236) as per the
817 manufacturer's protocol. In brief, single cells were sorted into PBS + 0.1% BSA,
818 washed twice and counted using a Bio-Rad TC20. 10,769 cells were added to each lane
819 of the 10X chip. The cells were then partitioned into Gel Beads in Emulsion in the
820 Chromium™ instrument, where cell lysis and barcoded reverse transcription of RNA
821 occurred, followed by amplification, fragmentation and 5' adaptor and sample index
822 attachment. Libraries were sequenced on an Illumina HiSeq 4000.

823 **Computational Analysis**

824 In total, we analysed 67,494 human cells from healthy (n=5) and cirrhotic (n=5) livers,
825 30,741 PBMCs from cirrhotic patients (n=4) and compared our data with a publicly-
826 available reference dataset of 8,381 PBMCs from a healthy donor.

827

828 *Pre-processing scRNA-seq data*

829 We aligned to the GRCh38 and mm10 (Ensembl 84) reference genomes as appropriate
830 for the input dataset, and estimated cell-containing partitions and associated UMIs,
831 using the Cell Ranger v2.1.0 Single-Cell Software Suite from 10X Genomics. Genes
832 expressed in fewer than three cells in a sample were excluded, as were cells that
833 expressed fewer than 300 genes or mitochondrial gene content >30% of the total UMI
834 count. We normalised by dividing the UMI count per gene by the total UMI count in
835 the corresponding cell and log-transforming. Variation in UMI counts between cells
836 was regressed according to a negative binomial model, prior to scaling and centering
837 the resulting value by subtracting the mean expression of each gene and dividing by its
838 standard deviation (E_n), then calculating $\ln(10^4 * E_n + 1)$.

839 *Dimensionality reduction, clustering, and DE analysis*

840 We performed unsupervised clustering and differential gene expression analyses in the
841 *Seurat* R package v2.3.0³⁹. In particular we used SNN graph-based clustering, where
842 the SNN graph was constructed using from 2 to 11 principal components as determined
843 by dataset variability shown in principal components analysis (PCA); the resolution
844 parameter to determine the resulting number of clusters was also tuned accordingly. To
845 assess cluster similarity we used the *BuildClusterTree* function from *Seurat*.

846 In total, we present scRNA-seq data from ten human liver samples (named Healthy 1-
847 5 and Cirrhotic 1-5), five human blood samples (n=4 cirrhotic named Blood 1-4 and
848 n=1 healthy named PBMC8K; pbmc8k dataset sourced from single-cell gene
849 expression datasets hosted by 10X Genomics), and two mouse liver samples (n=3
850 uninjured and n=3 fibrotic). For seven human liver samples (Healthy 1-4 and Cirrhotic
851 1-3) we performed scRNA-seq on both leucocytes (CD45⁺) and other non-parenchymal
852 cells (CD45⁻); for the remaining three human livers (Healthy 5, Cirrhotic 4-5) we
853 performed scRNA-seq on leucocytes only (Extended Data Fig. 2e, f).

854 Initially, we combined all human scRNA-seq datasets (liver and blood) and performed
855 clustering analysis with the aim of isolating a population of liver-resident cells, by
856 identifying contaminating circulatory cells within datasets generated from liver digests
857 and removing them from downstream analysis. Specifically, we removed from our liver
858 datasets cells that fell into clusters 1 and 13 of the initial dataset in Extended Data Fig.
859 1d.

860 Using further clustering followed by signature analysis, we interrogated this post-
861 processed liver-resident cell dataset for robust cell lineages. These lineages were
862 isolated into individual datasets, and the process was iterated to identify robust lineage
863 subpopulations. At each stage of this process we removed clusters expressing more than
864 one unique lineage signature in more than 25% of their cells from the dataset as
865 probable doublets. This resulted in removal of 1,351 cells. Where the cell proliferation
866 signature identified distinct cycling subpopulations, we re-clustered these again to
867 ascertain the identity of their constituent cells.

868 The murine scRNA-seq datasets were combined, clustered, and interrogated for cell
869 lineages in a similar manner as their human counterparts.

870 All heatmaps, t-SNE and UMAP visualisations, violin plots, and dot plots were
871 produced using *Seurat* functions in conjunction with the *ggplot2*, *pheatmap*, and *grid*
872 R packages. t-SNE and UMAP visualisations were constructed using the same number
873 of principal components as the associated clustering, with perplexity ranging from 30
874 to 300 according to the number of cells in the dataset or lineage. We conducted
875 differential gene expression analysis in *Seurat* using the standard AUC classifier to
876 assess significance. We retained only those genes with a log-fold change of at least 0.25
877 and expression in at least 25% of cells in the cluster under comparison.

878 *Defining cell lineage signatures*

879 For each cell we obtained a signature score across a curated list of known marker genes
880 per cell lineage in the liver (Supplementary Table 2). This signature score was defined
881 as the geometric mean of the expression of the associated signature genes in that cell.
882 Lineage signature scores were scaled from 0 to 1 across the dataset, and the score for
883 each cell with signature less than a given threshold (the mean of said signature score
884 across the entire dataset) was set as 0.

885 *Batch effect and quality control*

886 To investigate agreement between samples we extracted the average expression profile
887 for a given cell lineage in each sample, and calculated the Pearson correlation
888 coefficients between all possible pairwise comparisons of samples per lineage⁴⁰.

889 *Imputing dropout in T cell and ILC clusters*

890 To impute dropout of low-abundance transcripts in our T cell and ILC clusters so that
891 we might associate them with known subpopulations, we down-sampled to 7,380 cells
892 from 36,900 and applied the *scImpute* R package v0.0.8⁴¹, using as input both our
893 previous annotation labels and k-means spectral clustering (k=5), but otherwise default
894 parameters.

895 *Analysing functional phenotypes of scar-associated cells*

896 For further analysis of function we adopted the self-organising maps (SOM) approach
897 as implemented in the *SCRAT* R package v1.0.0⁴². For each lineage of interest we
898 constructed a SOM in *SCRAT* using default input parameters and according to its
899 clusters. We defined the signatures expressed in a cell by applying a threshold criterion

900 ($e^{\text{thresh}} = 0.95 \times e^{\text{max}}$) selecting the highest-expressed metagenes in each cell, and
901 identified for further analysis those metagene signatures defining at least 30% of cells
902 in at least one cluster within the lineage. We smoothed these SOMs using the
903 *disaggregate* function from the *raster* R package for visualisation purposes, and scaled
904 radar plots to maximum proportional expression of the signature. Gene ontology
905 enrichment analysis on the genes in these spots was performed using PANTHER 13.1
906 (pantherdb.org).

907 *Inferring injury dynamics and transcriptional regulation*

908 To generate cellular trajectories (pseudotemporal dynamics) we used the *monocle* R
909 package v2.6.1⁴³. We ordered cells in a semi-supervised manner based on their *Seurat*
910 clustering, scaled the resulting pseudotime values from 0 to 1, and mapped them onto
911 either the t-SNE or UMAP visualisations generated by *Seurat* or diffusion maps as
912 implemented in the *scater* R package v1.4.0⁴⁴ using the top 500 variable genes as input.
913 We removed mitochondrial and ribosomal genes from the geneset for the purposes of
914 trajectory analysis. Differentially-expressed genes along this trajectory were identified
915 using generalised linear models via the *differentialGeneTest* function in *monocle*.

916 When determining significance for differential gene expression along the trajectory, we
917 set a q-value threshold of $1e^{-20}$. We clustered these genes using hierarchical clustering
918 in *heatmap*, cutting the tree at $k=3$ to obtain gene modules with correlated gene
919 expression across pseudotime. Cubic smoothing spline curves were fitted to scaled gene
920 expression along this trajectory using the *smooth.spline* command from the *stats* R
921 package, and gene ontology enrichment analysis again performed using PANTHER
922 13.1.

923 We verified the trajectory and its directionality using the *velocyto* R package v0.6.0¹⁷,
924 estimating cell velocities from their spliced and unspliced mRNA content. We
925 generated annotated spliced and unspliced reads from the 10X BAM files via the
926 *dropEst* pipeline, before calculating gene-relative velocity using kNN pooling with
927 $k=25$, determining slope gamma with the entire range of cellular expression, and fitting
928 gene offsets using spanning reads. Aggregate velocity fields (using Gaussian smoothing
929 on a regular grid) and transition probabilities per lineage subpopulations were
930 visualised on t-SNE, UMAP, or diffusion map visualisations as generated previously.

931 Gene-specific phase portraits were plotted by calculating spliced and unspliced mRNA
932 levels against steady-state inferred by a linear model; levels of unspliced mRNA above
933 and below this steady-state indicate increasing and decreasing expression of said gene,
934 respectively. Similarly we plotted unspliced count signal residual per gene, based on
935 the estimated gamma fit, with positive and negative residuals indicating expected
936 upregulation and downregulation respectively.

937 For transcription factor analysis, we obtained a list of all genes identified as acting as
938 transcription factors in humans from AnimalTFDB⁴⁵. To further analyse transcription
939 factor regulons, we adopted the *SCENIC* v0.1.7 workflow in R⁴⁶, using default
940 parameters and the normalised data matrices from *Seurat* as input. For visualisation, we
941 mapped the regulon activity (AUC) scores thus generated to the pseudotemporal
942 trajectories from *monocle* and the clustering subpopulations from *Seurat*.

943 *Analysing inter-lineage interactions within the fibrotic niche*

944 For comprehensive systematic analysis of inter-lineage interactions within the fibrotic
945 niche we used CellPhoneDB²⁷. CellPhoneDB is a manually curated repository of
946 ligands, receptors, and their interactions, integrated with a statistical framework for
947 inferring cell-cell communication networks from single-cell transcriptomic data. In
948 brief, we derived potential ligand-receptor interactions based on expression of a
949 receptor by one lineage subpopulation and a ligand by another; as input to this algorithm
950 we used cells from the fibrotic niche as well as liver sinusoidal endothelial cells and
951 Kupffer cells as control, and we considered only ligands and receptors expressed in
952 greater than 5% of the cells in any given subpopulation. Subpopulation-specific
953 interactions were identified as follows: 1) randomly permuting the cluster labels of all
954 cells 1000 times and determining the mean of the average receptor expression of a
955 subpopulation and the average ligand expression of the interacting subpopulation, thus
956 generating a null distribution for each ligand-receptor pair in each pairwise comparison
957 between subpopulations, 2) calculating the proportion of these means that were "as or
958 more extreme" than the actual mean, thus obtaining a p-value for the likelihood of
959 subpopulation specificity for a given ligand-receptor pair, 3) prioritising interactions
960 that displayed specificity to subpopulations interacting within the fibrotic niche.

961 *Canonical correlation analysis*

962 To compare human and murine populations of monocytic phagocytes, we used
963 canonical correlation analysis as implemented in *Seurat*¹⁸. We map the genes in the
964 human dataset to their murine orthologues using *biomaRt*, discarding any genes for
965 which no orthologues can be found. We then calculate the shared low-dimensional
966 subspace on the union of genes that are variably expressed in both datasets (n=159),
967 and align using six canonical components as determined by evaluating the biweight
968 midcorrelation. Results are visualised on t-SNEs as previously described.

969 *Deconvolution of whole liver microarray data*

970 To assess macrophage composition early-stage NAFLD, we performed deconvolution
971 analysis on publicly available microarray data from annotated liver biopsy specimens
972 taken across the NAFLD disease spectrum (GEO accession GSE48452)²⁰. Tissue MP
973 cells from our human scRNA-seq data were manually clustered into the main annotated
974 MP populations. Signature gene expression profiles of SAM Φ , TMo, KC were used to
975 deconvolve the monocyte-macrophage composition of liver biopsy samples from
976 GSE48452 using Cibersort⁴⁷, as previously described¹⁹. The monocyte-macrophage
977 composition of each biopsy sample was then compared to the associated histological
978 and demographic features, available from the GEO database.

979 **Statistics and Reproducibility**

980 To assess whether our identified subpopulations were significantly overexpressed in
981 injury, we posited the proportion of injured cells in each cluster as a random count
982 variable using a Poisson process, as previously described⁴⁰. We modelled the rate of
983 detection using the total number of cells in the lineage profiled in a given sample as an
984 offset, with the condition of each sample (healthy vs cirrhotic) provided as a covariate
985 factor. The model was fitted using the R command *glm* from the *stats* package. The *P*
986 value for the significance of the proportion of injured cells was assessed using a Wald
987 test on the regression coefficient.

988 Remaining statistical analyses were performed using GraphPad Prism (GraphPad
989 Software, USA). Comparison of changes between two groups was performed using a
990 Mann-Whitney test (unpaired; two-tailed) or using a Wilcoxon matched-pairs signed
991 rank test (paired; two-tailed). Comparison of changes between multiple groups was

992 performed using a Kruskal-Wallis and Dunn, one-way ANOVA and Tukey or repeated
993 measures one-way ANOVA and Tukey tests. Correlations were performed using
994 Pearson correlation and best fit line plotted using linear regression. *P* values<0.05 were
995 considered statistically significant. All immunofluorescence stains were repeated in a
996 minimum of 3 patients and representative images are displayed.
997

998 **Methods References**

- 999 29. Searle, B. C., Gittelman, R. M., Manor, O. & Akey, J. M. Detecting sources of
1000 transcriptional heterogeneity in large-scale RNA-seq data sets. *Genetics* **204**,
1001 1391–1396 (2016).
- 1002 30. Bain, C. C. *et al.* Long-lived self-renewing bone marrow-derived macrophages
1003 displace embryo-derived cells to inhabit adult serous cavities. *Nat. Commun.* **7**,
1004 ncomms11852 (2016).
- 1005 31. Heinrich, M. C. *et al.* Crenolanib Inhibits the Drug-Resistant PDGFRA D842V
1006 Mutation Associated with Imatinib-Resistant Gastrointestinal Stromal Tumors.
1007 *Clin. Cancer Res.* **18**, 4375–4384 (2012).
- 1008 32. Patten, D. A. *et al.* SCARF-1 promotes adhesion of CD4+ T cells to human
1009 hepatic sinusoidal endothelium under conditions of shear stress. *Sci. Rep.* **7**,
1010 17600 (2017).
- 1011 33. Schindelin, J. *et al.* Fiji: an open-source platform for biological-image analysis.
1012 *Nat. Methods* **9**, 676–682 (2012).
- 1013 34. Bankhead, P. *et al.* QuPath: Open source software for digital pathology image
1014 analysis. *Sci. Rep.* **7**, 16878 (2017).
- 1015 35. Arganda-Carreras, I. *et al.* Trainable Weka Segmentation: A machine learning
1016 tool for microscopy pixel classification. *Bioinformatics* **33**, 2424–2426 (2017).
- 1017 36. Kleiner, D. E. *et al.* Design and validation of a histological scoring system for
1018 nonalcoholic fatty liver disease. *Hepatology* **41**, 1313–1321 (2005).
- 1019 37. Deroulers, C. *et al.* Analyzing huge pathology images with open source
1020 software. *Diagn. Pathol.* **8**, 92 (2013).
- 1021 38. Kendall, T. J. *et al.* Hepatic elastin content is predictive of adverse outcome in
1022 advanced fibrotic liver disease. *Histopathology* **73**, 90–100 (2018).
- 1023 39. Satija, R., Farrell, J. A., Gennert, D., Schier, A. F. & Regev, A. Spatial
1024 reconstruction of single-cell gene expression data. *Nat. Biotechnol.* **33**, 495–
1025 502 (2015).
- 1026 40. Haber, A. L. *et al.* A single-cell survey of the small intestinal epithelium.
1027 *Nature* (2017). doi:10.1038/nature24489
- 1028 41. Li, W. V. & Li, J. J. An accurate and robust imputation method scImpute for
1029 single-cell RNA-seq data. *Nat. Commun.* **9**, 997 (2018).

- 1030 42. Camp, J. G. *et al.* Multilineage communication regulates human liver bud
1031 development from pluripotency. *Nature* **546**, 533–538 (2017).
- 1032 43. Trapnell, C. *et al.* The dynamics and regulators of cell fate decisions are
1033 revealed by pseudotemporal ordering of single cells. *Nat. Biotechnol.* **32**, 381–
1034 386 (2014).
- 1035 44. McCarthy, D. J., Campbell, K. R., Lun, A. T. L. & Wills, Q. F. Scater: Pre-
1036 processing, quality control, normalization and visualization of single-cell RNA-
1037 seq data in R. *Bioinformatics* **33**, 1179–1186 (2017).
- 1038 45. Zhang, H. M. *et al.* AnimalTFDB 2.0: A resource for expression, prediction
1039 and functional study of animal transcription factors. *Nucleic Acids Res.* **43**,
1040 D76–D81 (2015).
- 1041 46. Aibar, S. *et al.* SCENIC: Single-cell regulatory network inference and
1042 clustering. *Nat. Methods* **14**, 1083–1086 (2017).
- 1043 47. Newman, A. M. *et al.* Robust enumeration of cell subsets from tissue
1044 expression profiles. *Nat. Methods* (2015). doi:10.1038/nmeth.3337

1045 **Data and materials availability**

1046 Our expression data will be freely available for user-friendly interactive browsing
1047 online at <http://www.livercellatlas.mvm.ed.ac.uk>. CellPhoneDB is available at
1048 www.CellPhoneDB.org. All raw sequencing data will be deposited in the Gene
1049 Expression Omnibus (GEO accession GSE136103).

1050 **Code availability**

1051 R scripts enabling the main steps of the analysis are available from the corresponding
1052 authors on reasonable request.

1053 **Acknowledgements**

1054 This work was supported by an MRC Clinician Scientist Fellowship (MR/N008340/1)
1055 to P.R., a Wellcome Trust Senior Research Fellowship in Clinical Science (ref. 103749)
1056 to N.C.H., an AbbVie Future Therapeutics and Technologies Division grant to N.C.H.,
1057 a Guts UK– Children's Liver Disease Foundation grant (ref. R43927) to N.C.H., a
1058 Tenovus Scotland grant (ref. E18/05) to R.D. and N.C.H., and British Heart Foundation

1059 grants (RM/17/3/33381; RE/18/5/34216) to N.C.H. R.V-T. was funded by EMBO and
1060 Human Frontiers long-term fellowships. C.J.W. was funded by a BBSRC New
1061 Investigator Award (BB/N018869/1). P.N.N., C.J.W. and N.T.L. are funded by the
1062 NIHR Birmingham Biomedical Research Centre at the University Hospitals
1063 Birmingham NHS Foundation Trust and the University of Birmingham. This paper
1064 presents independent research supported by the NIHR Birmingham Biomedical
1065 Research Centre at the University Hospitals Birmingham NHS Foundation Trust and
1066 the University of Birmingham. The views expressed are those of the author(s) and not
1067 necessarily those of the NHS, the NIHR or the Department of Health and Social Care.
1068 J.P.I. is funded by the NIHR Bristol Biomedical Research Centre, University Hospitals
1069 Bristol Foundation Trust and the University of Bristol. This work was also supported
1070 by Wellcome Sanger core funding (WT206194). We thank the patients who donated
1071 liver tissue and blood for this study. We thank J. Davidson, C. Ibbotson, J. Black and
1072 A. Baird of the Scottish Liver Transplant Unit and the research nurses of the Wellcome
1073 Trust Clinical Research Facility for assistance with consenting patients for this study.
1074 We thank the liver transplant coordinators and surgeons of the Scottish Liver Transplant
1075 Unit and the surgeons and staff of the Hepatobiliary Surgical Unit, Royal Infirmary of
1076 Edinburgh for assistance in procuring human liver samples. We thank S. Johnston, W.
1077 Ramsay and M. Pattison (QMRI Flow Cytometry and Cell Sorting Facility, University
1078 of Edinburgh) for technical assistance with fluorescence activated cell sorting (FACS)
1079 and flow cytometry. We thank Jon Henderson for technical support and Gillian
1080 Muirhead for assistance with liver endothelial cell isolation. This publication is part of
1081 the Human Cell Atlas (www.humancellatlas.org/publications).

1082 **Author Contributions**

1083 P.R. performed experimental design, tissue procurement, data generation, data analysis
1084 and interpretation, and manuscript preparation; R.D. performed experimental design,
1085 data generation and data analysis; E.D., K.P.M., B.E.P.H., M.B., J.A.M. and N.T.L.
1086 performed data generation and analysis; J.R.P. generated the interactive online browser;
1087 M.E. and R.V-T. assisted with CellPhoneDB analyses and critically appraised the
1088 manuscript; T.J.K. performed pathological assessments and provided intellectual
1089 contribution; N.O.C., J.A.F. and P.N.N. provided intellectual contribution; C.J.W.
1090 performed tissue procurement, data generation, interpretation and intellectual

1091 contribution; J.R.W-K. performed computational analysis with assistance from J.R.P
1092 and R.S.T. and advice from C.P.P., J.M. and S.A.T.; J.R.W-K. also helped with
1093 manuscript preparation and C.P.P., J.M. and S.A.T. critically appraised the manuscript;
1094 E.M.H., D.J.M. and S.J.W. procured human liver tissue and critically appraised the
1095 manuscript. J.P.I., F.T. and J.W.P. provided intellectual contribution and critically
1096 appraised the manuscript; N.C.H. conceived the study, designed experiments,
1097 interpreted data and prepared the manuscript.

1098 **Author Information**

1099 The authors declare no competing financial interests. Address correspondence or
1100 requests for materials to Prakash Ramachandran or Neil Henderson.

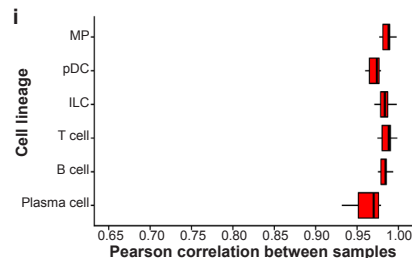
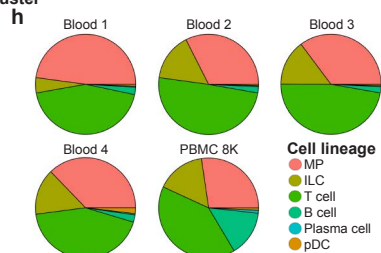
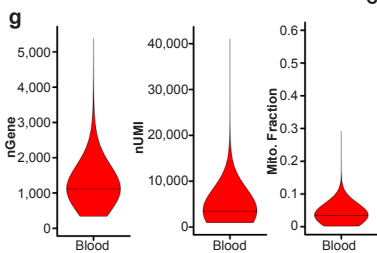
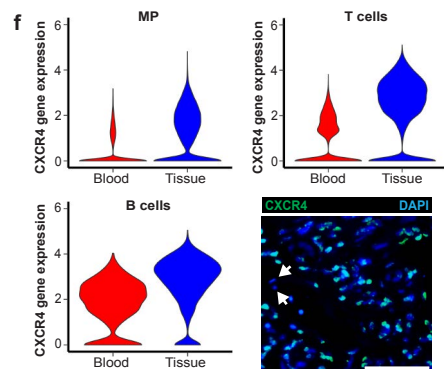
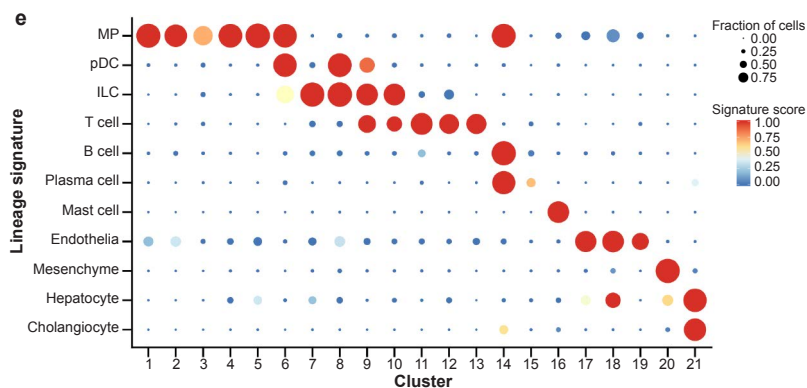
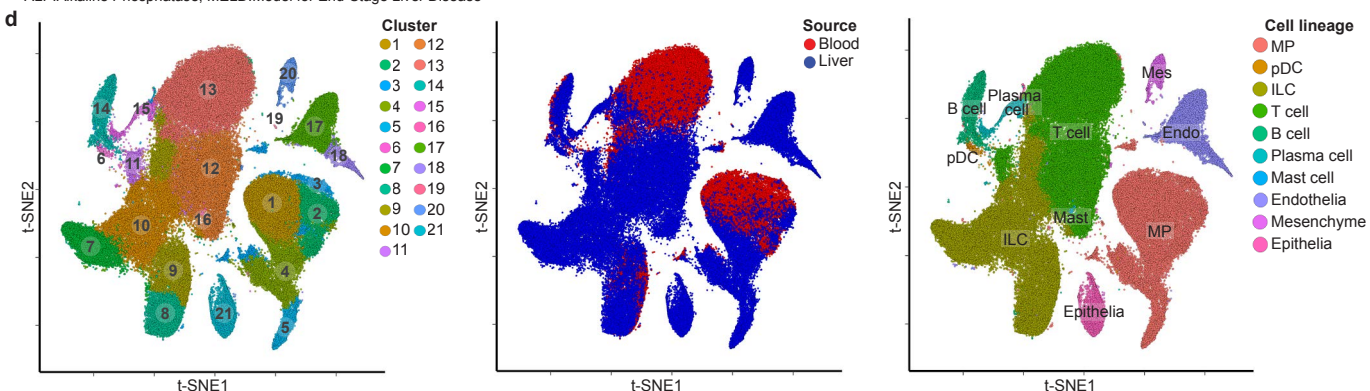
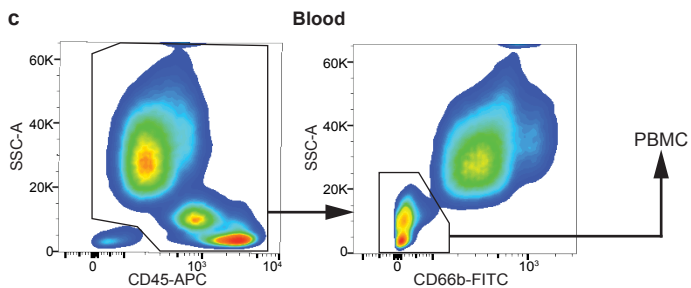
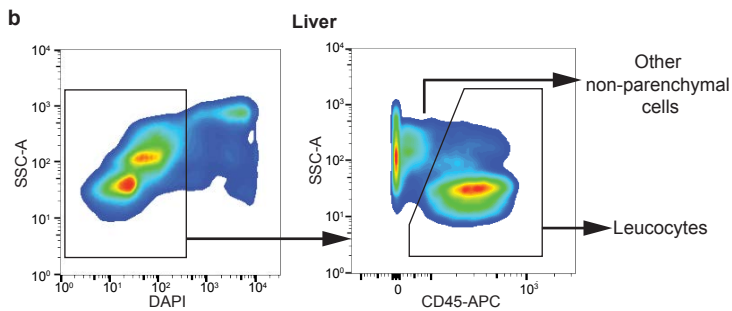
1101 **Extended Data Figure 1: Strategy for isolation of human liver non-parenchymal**
1102 **cells.**

1103 **a**, Patient demographics and clinical information, Mean±SEM. **b**, Flow cytometry
1104 gating strategy for isolating leucocytes (CD45⁺) and other non-parenchymal cells
1105 (CD45⁻) from human liver, representative plots from 10 livers. **c**, Flow cytometry plots:
1106 gating strategy for isolating peripheral blood mononuclear cells (PBMC),
1107 representative plots from 4 patients. **d**, Clustering 103,568 cells from 5 healthy human
1108 livers, 5 cirrhotic human livers, 1 healthy PBMC and 4 cirrhotic PBMC (left),
1109 annotating source (PBMC *versus* liver; middle) and cell lineage inferred from known
1110 marker gene signatures (right). Endo, endothelial cell; ILC, innate lymphoid cell; Mast,
1111 mast cell; Mes, mesenchymal cell; MP, mononuclear phagocyte; pDC, plasmacytoid
1112 dendritic cell. **e**, Dotplot: annotating PBMC and liver clusters by lineage signatures.
1113 Circle size indicates cell fraction expressing signature greater than mean; colour
1114 indicates mean signature expression (red, high; blue, low). **f**, CXCR4 gene expression
1115 in single cells derived from blood or liver tissue, divided by cell lineage. Representative
1116 immunofluorescence micrograph, human liver: CXCR4 (green), DAPI (blue), arrows
1117 CXCR4⁻ cells in the lumen of a blood vessel. Scale bar 50µm. **g**, Violin plots: number
1118 of unique genes (nGene), number of total Unique Molecular Identifiers (nUMI) and
1119 mitochondrial gene fraction expressed in 5 PBMC samples; Black line, median. **g**, Pie
1120 charts: proportion of cell lineage per PBMC sample. **h**, Box and whisker plot:
1121 agreement in expression profiles across 5 PBMC samples. Pearson correlation
1122 coefficients between average expression profiles for cell in each lineage, across all pairs
1123 of samples. Black bar, median value; box edges, 25th and 75th percentiles; whiskers, full
1124 range.

a

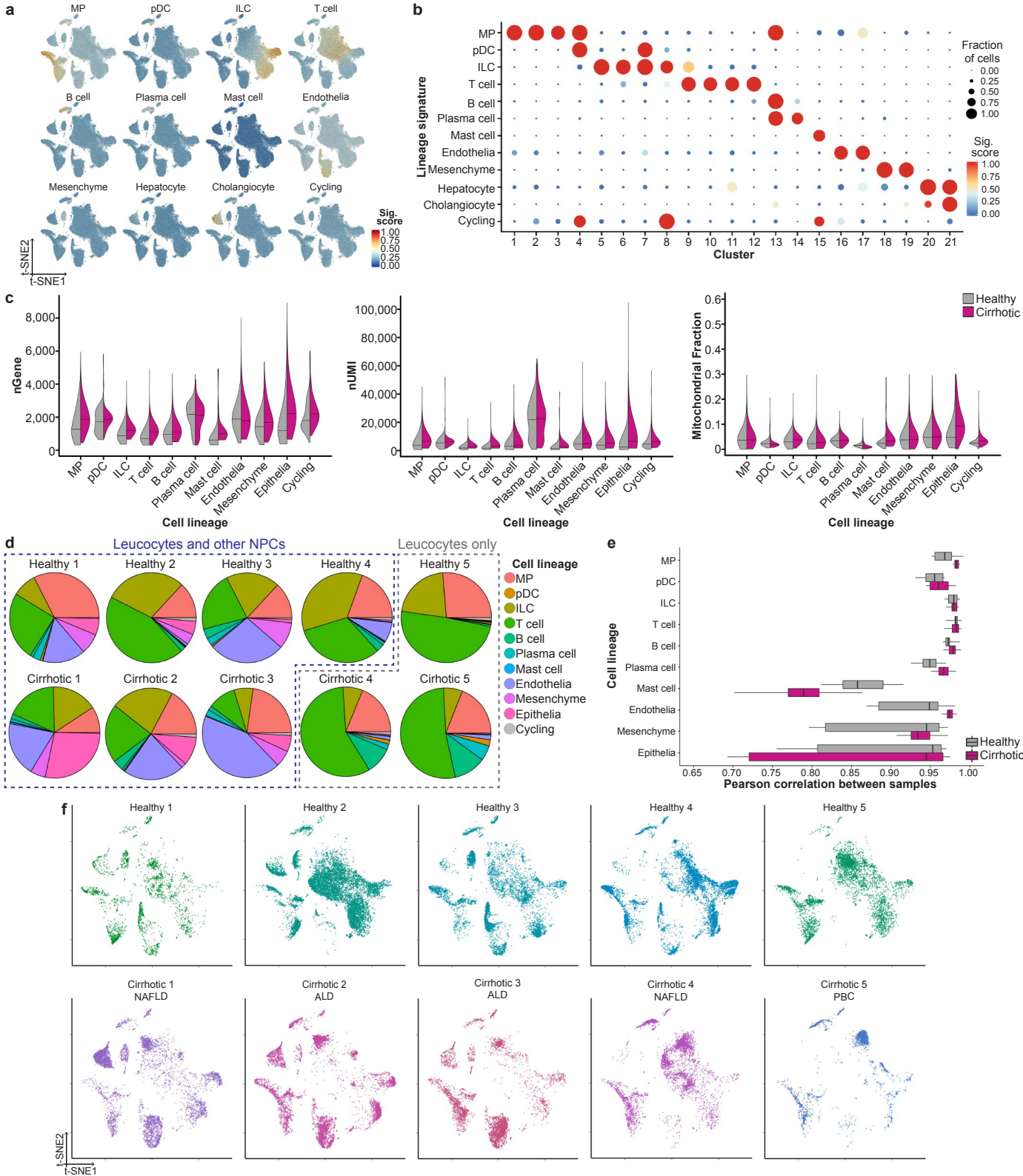
	Healthy liver (n=5)	Cirrhotic liver (n=5)	Blood (n=4)
Age (yrs)	57.4±7.9	56.6±5.8	63.2±3.8
Gender (M:F)	4:1	3:2	3:1
Aetiology of liver disease	N/A	2xNAFLD 2xALD 1xPBC	3xNAFLD 1xHH
Haemoglobin (g/l)	145±14	106±17	131±2.1
White Cell Count (x10 ⁹ /l)	8.2±2.2	5.9±1.7	3.7±1.5
Platelets (x10 ⁹ /l)	300±91	137±56	73±38
Prothrombin Time (s)	11.6±1.1	19.6±3.8	16.0±3.6
Creatinine (µmol/l)	76.4±14.5	96.8±28.6	74.5±9.7
Na ⁺ (mmol/l)	141±2.6	131±7.0	139±2.1
Bilirubin (µmol/l)	10±5.2	79.6±83.5	36.3±20.0
ALT (IU/l)	27.8±19.3	77.8±80.7	96.2±121.0
ALP (IU/l)	122±47	140±80	203±153
MELD Score	6.6±0.5	17.3±4.5	11.7±4.3

NAFLD:Non-alcoholic fatty liver disease; ALD:Alcohol-related liver disease; PBC:Primary biliary cholangitis; HH:Hereditary haemochromatosis; ALT:Alanine transaminase; ALP:Alkaline Phosphatase; MELD:Model for End-Stage Liver Disease



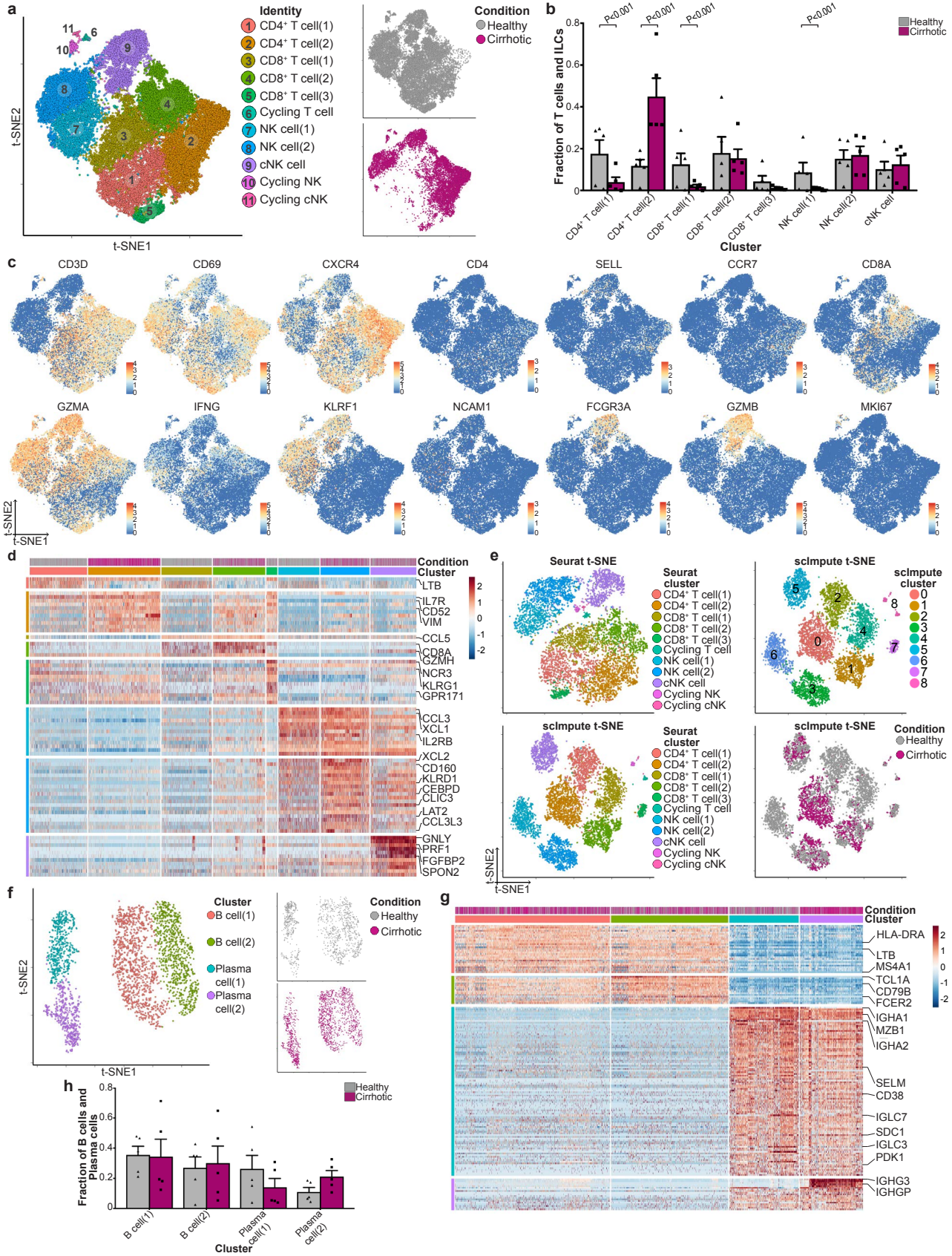
1125 **Extended Data Figure 2: Quality control and annotation of human liver-resident**
1126 **cells.**

1127 **a**, Lineage signature expression across 66,135 liver-resident cells from 5 healthy and 5
1128 cirrhotic human livers (red, high; blue, low). **b**, Dotplot: annotating liver-resident cell
1129 clusters by lineage signature. Circle size indicates cell fraction expressing signature
1130 greater than mean; colour indicates mean signature expression (red, high; blue, low). **c**,
1131 Violin plot: number of unique genes (nGene; left), number of total Unique Molecular
1132 Identifiers (nUMI; middle) and mitochondrial gene fraction (right) across 66,135 liver-
1133 resident cells from 5 healthy *versus* 5 cirrhotic livers; Black line, median. **d**, Pie charts:
1134 proportion of cell lineage per liver sample. **e**, Box and whisker plot: agreement in
1135 expression profiles across 5 healthy and 5 cirrhotic liver samples. Pearson correlation
1136 coefficients between average expression profiles for cell in each lineage, across all pairs
1137 of samples. Black bar, median value; box edges, 25th and 75th percentiles; whiskers,
1138 range. **f**, t-SNE visualisation: liver-resident cells per liver sample; Cirrhotic samples
1139 annotated by aetiology of underlying liver disease; NAFLD, Non-alcoholic fatty liver
1140 disease; ALD, Alcohol-related liver disease; PBC, Primary biliary cholangitis.



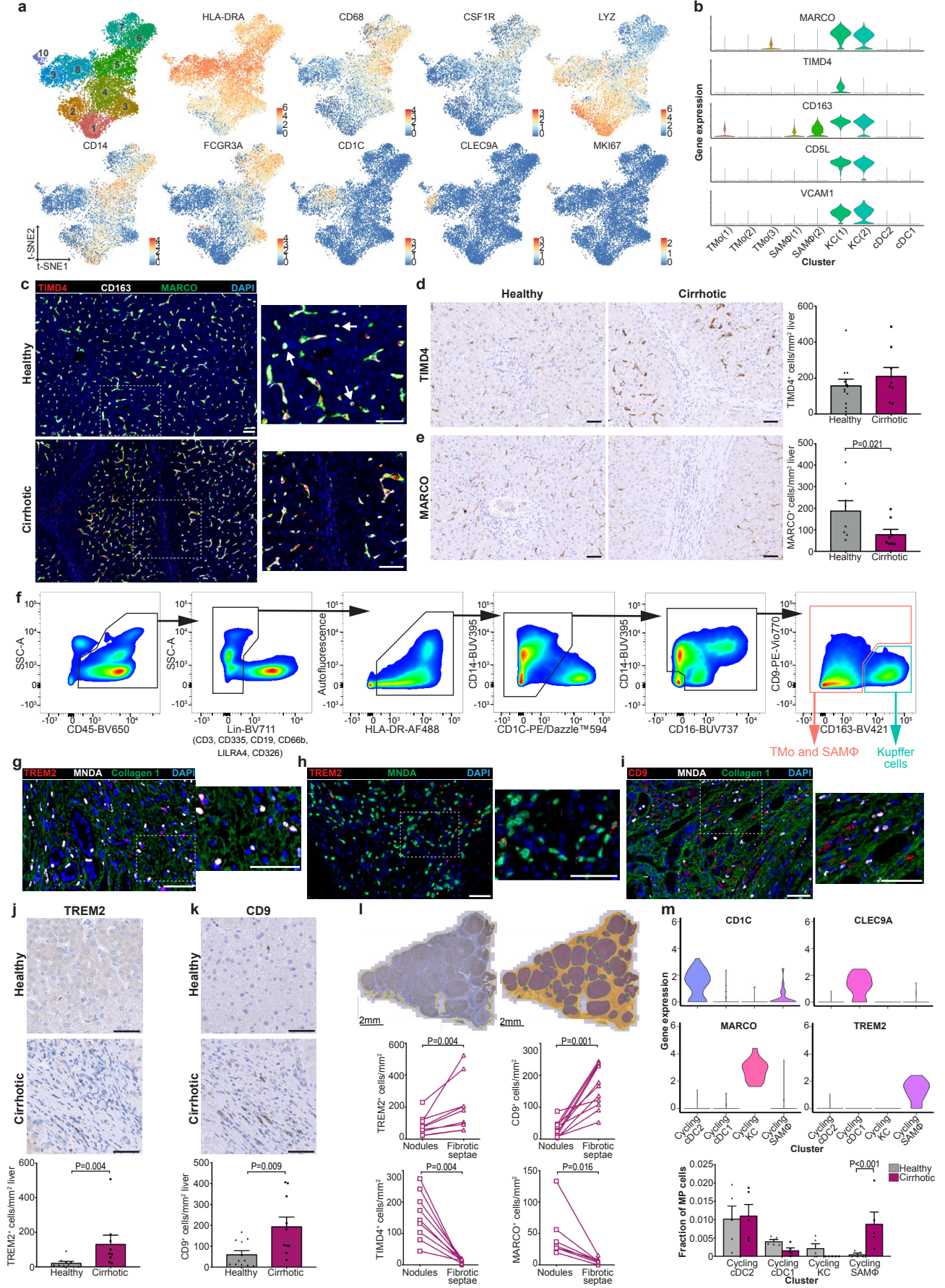
1141 **Extended Data Figure 3: Annotating human liver lymphoid cells.**

1142 **a**, Clustering and annotating 36,900 T cells and innate lymphoid cells (ILC) (left) from
1143 5 healthy and 5 cirrhotic human livers, annotating injury condition (right). cNK,
1144 cytotoxic NK cell. **b**, Fractions of T cell and ILC subpopulations in healthy (n=5) *versus*
1145 cirrhotic (n=5) livers, Mean±SEM, Wald. **c**, Selected gene expression in 36,900 T cells
1146 and ILC. **d**, Heatmap: T cell and ILC cluster marker genes (colour coded top by cluster
1147 and condition), exemplar genes labelled right. Cells columns, genes rows. **e**, t-SNE
1148 visualisations: downsampled T cell and ILC dataset (7,380 cells from 5 healthy and 5
1149 cirrhotic human livers) pre- and post-imputation; annotating data used for visualisation
1150 and clustering, inferred lineage, injury condition. No additional heterogeneity was
1151 observed following imputation. **f**, Clustering 2,746 B cells and plasma cells (left) from
1152 5 healthy and 5 cirrhotic human livers, annotating injury condition (right). **g**, Heatmap:
1153 B cell and plasma cell cluster marker genes (colour coded top by cluster and condition),
1154 exemplar genes labelled right. Cells columns, genes rows. **h**, Fractions of B cell and
1155 plasma cell subpopulations in healthy (n=5) *versus* cirrhotic (n=5) livers, Mean±SEM.



1156 **Extended Data Figure 4: Annotating human liver mononuclear phagocytes.**

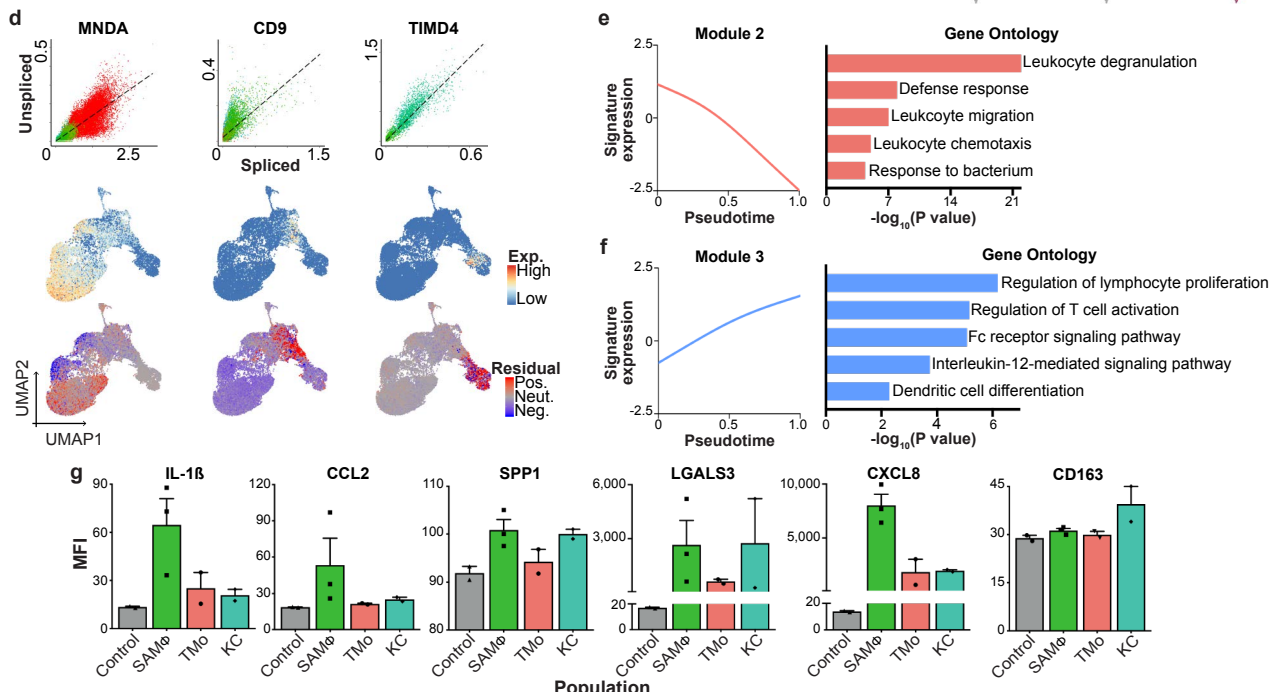
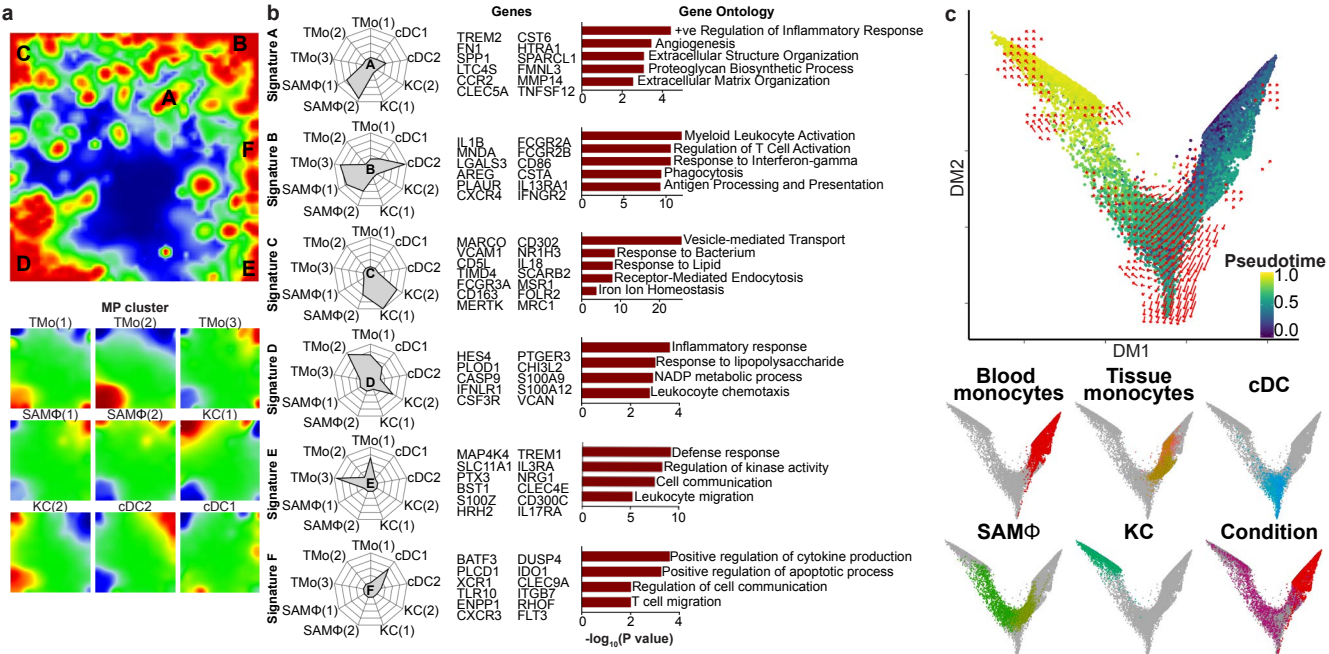
1157 **a**, Clustering and selected genes expressed in 10,737 mononuclear phagocytes (MP)
1158 from 5 healthy and 5 cirrhotic human livers. **b**, Scaled gene expression of Kupffer cell
1159 (KC) cluster markers across MP cells from healthy (n=5) and cirrhotic (n=5) livers. **c**,
1160 Representative immunofluorescence images, healthy *versus* cirrhotic liver: TIMD4
1161 (red), CD163 (white), MARCO (green), DAPI (blue), arrows
1162 CD163⁺MARCO⁺TIMD4⁻ cells, scale bars 50µm. **d**, TIMD4 immunohistochemistry,
1163 cell counts healthy (n=12) *versus* cirrhotic (n=9) liver, Mean±SEM, scale bars 50µm.
1164 **e**, MARCO immunohistochemistry, cell counts healthy (n=8) *versus* cirrhotic (n=8)
1165 liver, Mean±SEM, Mann-Whitney two-tailed, scale bars 50µm. **f**, Flow cytometry:
1166 gating strategy for identifying KC, TMo and SAMΦ in healthy (n=2) and cirrhotic
1167 (n=3) liver. SAMΦ are detected as TREM2+CD9+ cells within the TMo and SAMΦ
1168 gate (see Fig. 2f). **g**, Representative immunofluorescence image, cirrhotic liver:
1169 TREM2 (red), MNDA (white), collagen 1 (green), DAPI (blue), scale bars 50µm. **h**,
1170 Representative image, cirrhotic liver: TREM2 (smFISH; red), MNDA
1171 (immunofluorescence; green), DAPI (blue), scale bars 50µm. **i**, Representative
1172 immunofluorescence image, cirrhotic liver: CD9 (red), MNDA (white), collagen 1
1173 (green), DAPI (blue), scale bars 50µm. **j**, TREM2 immunohistochemistry, cell counts
1174 healthy (n=10) *versus* cirrhotic (n=9) liver, Mann-Whitney two-tailed, scale bars 50µm.
1175 **k**, CD9 immunohistochemistry, cell counts healthy (n=12) *versus* cirrhotic (n=10) liver,
1176 Mann-Whitney two-tailed, scale bars 50µm. **l**, Exemplar tissue segmentation of
1177 cirrhotic liver section into fibrotic septae (orange) and parenchymal nodules (purple)
1178 (top); TREM2 (n=9), CD9 (n=11), TIMD4 (n=9) and MARCO (n=7)
1179 immunohistochemistry and cell counts in parenchymal nodules *versus* fibrotic septae,
1180 Wilcoxon two-tailed. **m**, Clustering and annotation of 208 cycling MP cells from
1181 healthy (n=5) and cirrhotic (n=5) livers, scaled gene expression of MP subpopulation
1182 markers across 4 clusters of cycling MP cells (top), fractions of cycling MP
1183 subpopulations in 5 healthy *versus* 5 cirrhotic livers (bottom), Mean±SEM, Wald.



1184 **Extended Data Figure 5: Phenotypic characterisation of mononuclear**
1185 **phagocytes in healthy and cirrhotic human livers.**

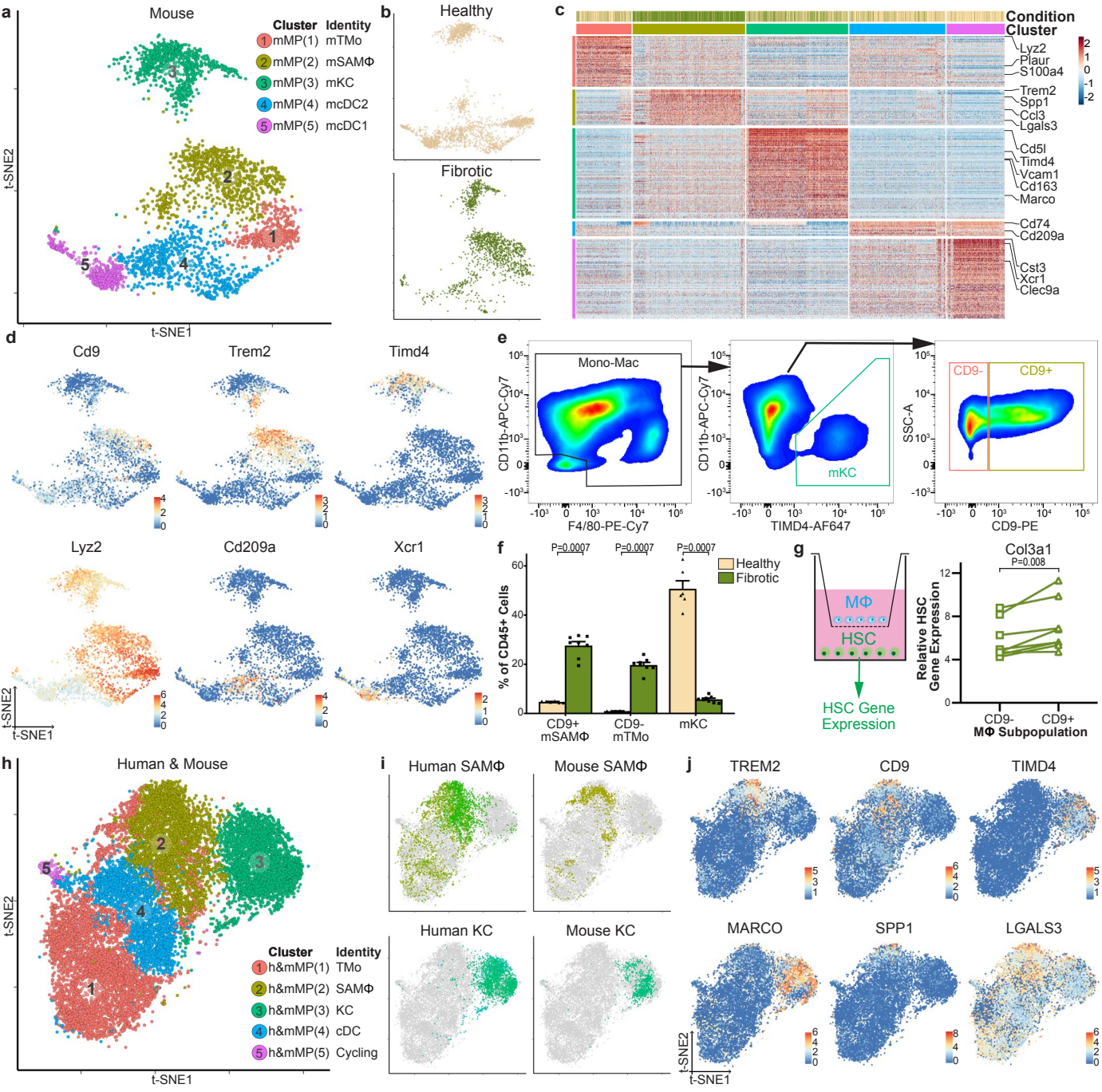
1186 **a**, Self-Organising Map (SOM; 60x60 grid): smoothed scaled metagene expression of
1187 10,737 mononuclear phagocyte (MP) cells from healthy (n=5) and cirrhotic (n=5)
1188 livers. 20,952 genes, 3,600 metagenes, 44 signatures. A-F label metagene signatures
1189 overexpressed in one or more MP subpopulations (top). Smoothed mean metagene
1190 expression profile for each MP subpopulation (bottom). **b**, Radar plots (left): metagene
1191 signatures A-F showing distribution of signature expression across MP subpopulations
1192 from 10,737 MP cells, exemplar genes (middle) and selected Gene Ontology (GO)
1193 enrichment (right), Fisher's exact test. **c**, Diffusion map visualisation, blood monocytes
1194 and liver-resident MP lineages (23,075 cells from healthy (n=5) and cirrhotic (n=5)
1195 liver samples and PBMCs (n=4), annotating *monocle* pseudotemporal dynamics (purple
1196 to yellow). RNA velocity field (red arrows) visualised using Gaussian smoothing on
1197 regular grid (top). Annotation of MP subpopulation, injury condition (bottom). **d**,
1198 Unspliced-spliced phase portraits (top row), 23,075 cells coloured and visualised as in
1199 Fig 3a, monocyte (*MNDA*), SAM Φ (*CD9*) and KC marker genes (*TIMD4*). Cells plotted
1200 above or below the steady-state (black dashed line) indicate increasing or decreasing
1201 expression of gene, respectively. Spliced expression profile for stated genes (middle
1202 row; red high, blue low). Unspliced residuals for stated genes (bottom row), positive
1203 (red) indicating expected upregulation, negative (blue) indicating expected
1204 downregulation. *MNDA* displays negative velocity in SAM Φ , *CD9* displays positive
1205 velocity in monocytes and SAM Φ , *TIMD4* velocity is restricted to KC. **e**, Cubic
1206 smoothing spline curve fitted to averaged expression of all genes in module 2 from
1207 blood monocyte-SAM Φ pseudotemporal trajectory (see Fig. 3c), selected GO
1208 enrichment (right), Fisher's exact test. **f**, Cubic smoothing spline curve fitted to
1209 averaged expression of all genes in module 3 from blood monocyte-cDC
1210 pseudotemporal trajectory (see Fig. 3c), selected GO enrichment (right), Fisher's exact
1211 test. **g**, Luminex assay: quantification of levels of stated proteins in culture medium
1212 from FACS-isolated scar-associated macrophages (SAM Φ , n=3), tissue monocytes
1213 (TMo, n=2), Kupffer cells (KC, n=2), and control (media alone, n=2), Mean \pm SEM,
1214 MFI median fluorescence intensity. **h**, Heatmap: transcription factor regulons across
1215 MP pseudotemporal trajectory and in KC (colour coded top by MP cluster, condition

1216 and pseudotime), selected regulons labelled right. Cells columns, regulons rows. **i**,
1217 Scaled regulon expression of selected regulons across MP clusters from healthy (n=5)
1218 and cirrhotic (n=5) livers.



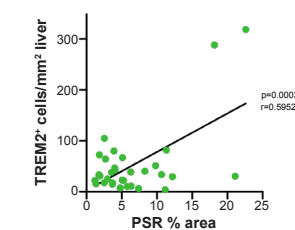
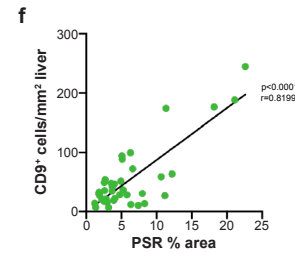
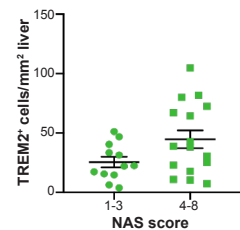
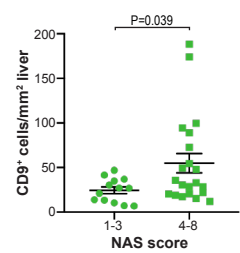
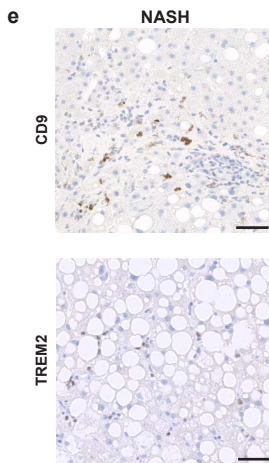
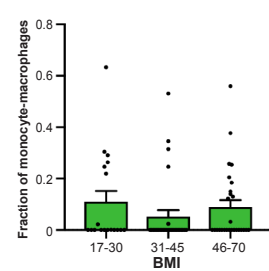
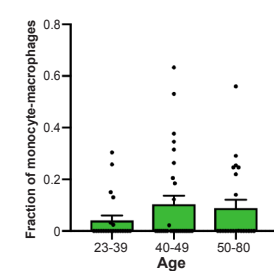
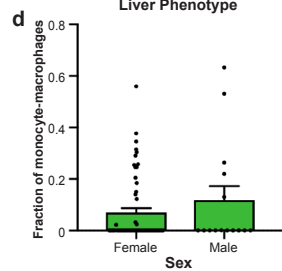
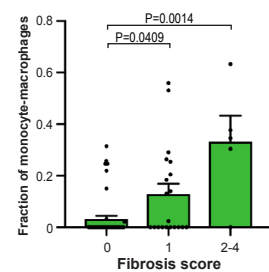
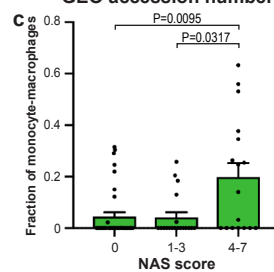
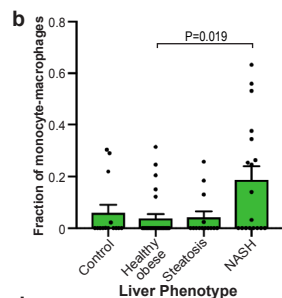
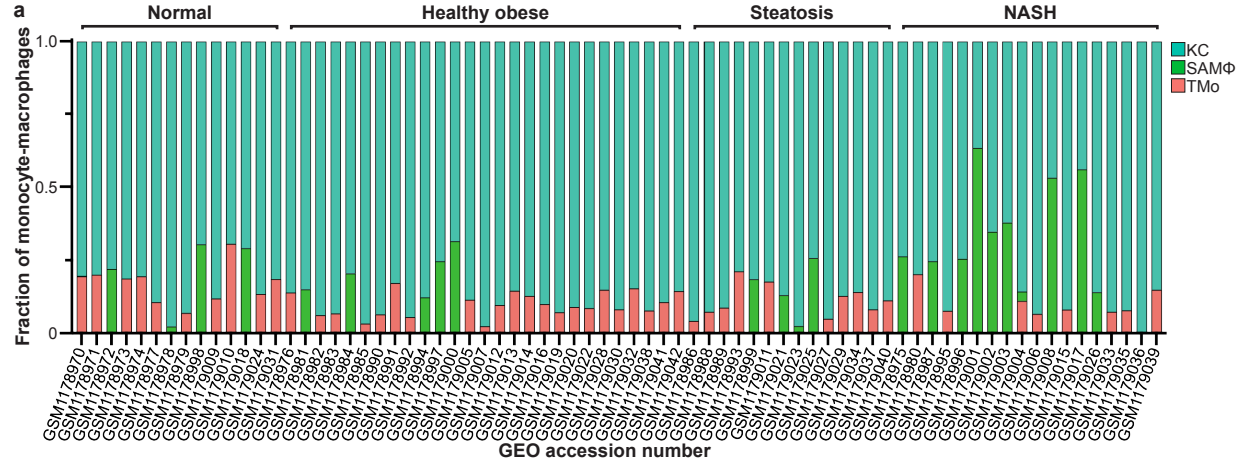
1219 **Extended Data Figure 6: Characterisation of macrophages in mouse liver**
1220 **fibrosis.**

1221 **a**, Clustering and annotating 3,250 mouse mononuclear phagocytes (mMP) from
1222 healthy (n=3) and fibrotic (4 weeks carbon tetrachloride treatment, n=3) livers. mTMo,
1223 tissue monocyte; mSAM Φ , scar-associated macrophage; mKC, Kupffer cell; mcDC,
1224 conventional dendritic cell. **b**, Annotating mMP cells by injury condition. **c**, Heatmap:
1225 mMP cluster marker genes (top, colour coded by cluster and condition), exemplar genes
1226 labelled (right). Cells columns, genes rows. **d**, Selected genes expressed in 3,250 mMP
1227 **e**, Flow cytometry: gating strategy for identifying KC, TMo and SAM Φ in healthy
1228 (n=2) and cirrhotic (n=3) liver. Flow cytometry plots: gating strategy for identifying
1229 mKC, CD9⁻ mTMo and CD9⁺ mSAM Φ in fibrotic mice (n=8 from 2 independent
1230 experiments). **f**, Quantifying mouse macrophage subpopulations by flow cytometry:
1231 healthy (n=6) and fibrotic (n=8) mouse livers from 2 independent experiments,
1232 macrophage subpopulation (x-axis) as a percentage of total viable CD45⁺ cells (y-axis),
1233 Mean \pm SEM, Mann-Whitney two-tailed. **g**, Hepatic stellate cell activation assay: co-
1234 culture of hepatic stellate cells (HSC) from uninjured mouse liver and FACS-isolated
1235 macrophage subpopulations (M Φ) from fibrotic mouse liver (left). Co-culture with
1236 CD9⁻ mTMo or CD9⁺ mSAM Φ isolated from 8 fibrotic mice (2 independent
1237 experiments), qPCR of Col3a1 in HSC, expression relative to mean expression of
1238 quiescent HSC (right), Wilcoxon two-tailed. **h**, Clustering 3,250 mouse mononuclear
1239 phagocytes (mMP) and 10,737 human mononuclear phagocytes (hMP) into 5 clusters
1240 using canonical correlation analysis (CCA). Annotation of cross-species clusters
1241 (identity). **i**, Annotation of human and mouse macrophage subpopulations from 3,250
1242 mMP and 10,737 hMP. **j**, Selected genes expressed in 3,250 mMP and 10,737 hMP.



1243 **Extended Data Figure 7: Scar-associated macrophage expansion in human**
1244 **NASH**

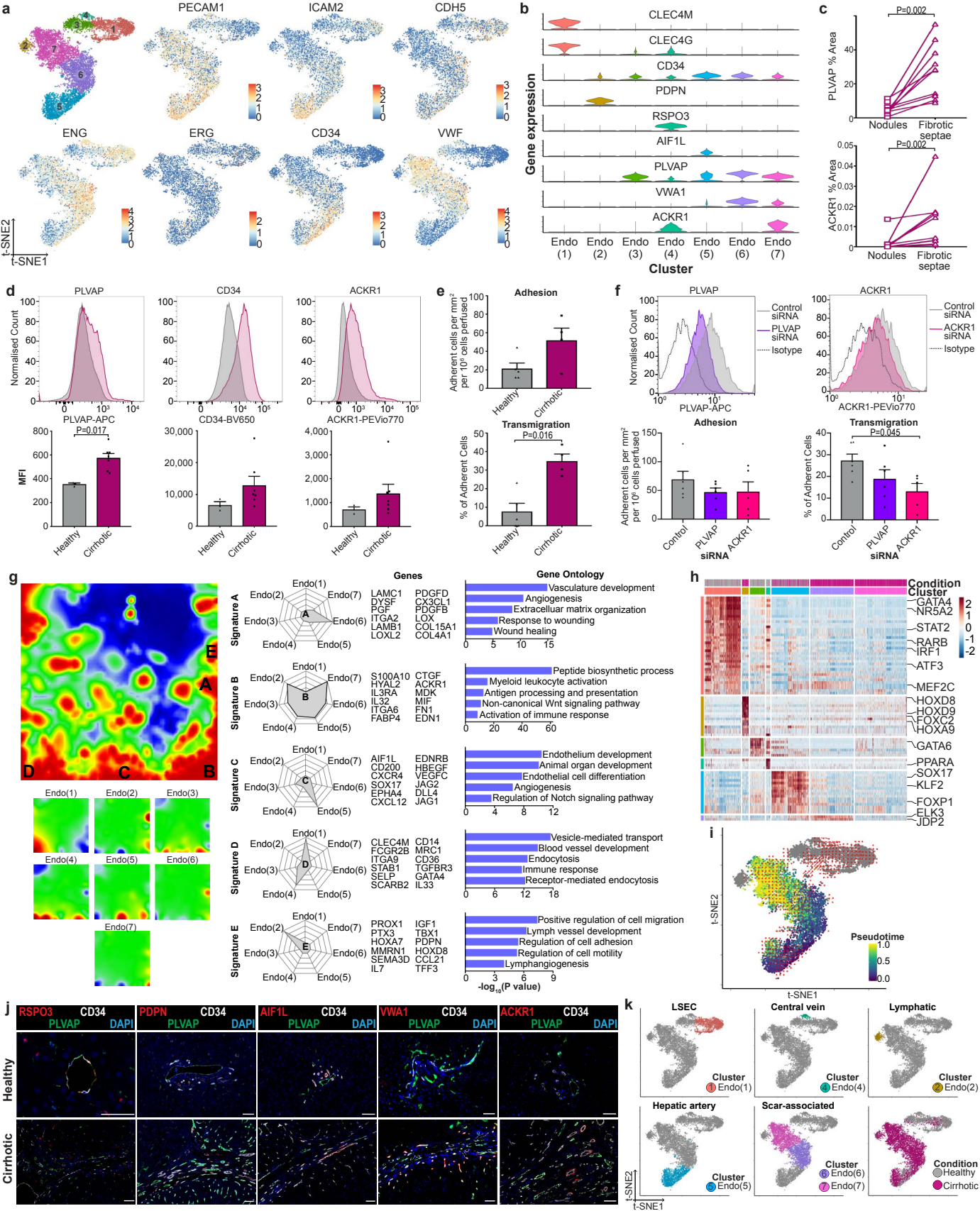
1245 **a to d**, Deconvolution: publicly available whole liver microarray data (n=73) assessed
1246 for frequency of scar-associated macrophages (SAM Φ), Kupffer cells (KC) and tissue
1247 monocytes (TMo) using Cibersort algorithm. **a**, Macrophage composition: x-axis, GEO
1248 accession number; y-axis, fraction of monocyte-macrophages; Top, annotated by liver
1249 phenotype; NASH, Non-alcoholic steatohepatitis. **b**, Frequency of SAM Φ in control
1250 (n=14), heathy obese (n=27), steatosis (n=14) and NASH (n=18) livers, Mean \pm SEM,
1251 Kruskal-Wallis and Dunn. **c**, Frequency of SAM Φ in patients with histological NAFLD
1252 activity score (NAS) of 0 (n=37), 1-3 (n=19) and 4-7 (n=17) (left). Frequency of SAM Φ
1253 in patients with histological fibrosis score of 0 (n=46), 1 (n=20) and 2-4 (n=5) (right),
1254 Mean \pm SEM, Kruskal-Wallis and Dunn. **d**, Frequency of SAM Φ in female (n=58) and
1255 male (n=15) patients (left). Frequency of SAM Φ in patients aged 23-39 (n=22), 40-49
1256 (n=29) and 50-80 (n=22) (middle). Frequency of SAM Φ in patients with a body mass
1257 index (BMI) of 17-30 (n=18), 31-45 (n=28) and 46-70 (n=27) (right). **e**, CD9 and
1258 TREM2 staining in NASH liver biopsy sections (left), Scale bars, 50 μ m. Cell counting
1259 (right): CD9 staining, NAS 1-3 (n=13) *versus* NAS 4-8 (n=21), Mean \pm SEM, Mann-
1260 Whitney two-tailed. TREM2 staining, NAS 1-3 (n=12) *versus* NAS 4-8 (n=16),
1261 Mean \pm SEM. **f**, Correlation of cell counts with picosirius red (PSR) digital
1262 morphometric pixel quantification in NAFLD liver biopsy tissue; CD9 staining (top;
1263 n=39); TREM2 staining (bottom; n=32); Pearson correlation and linear regression.



1264 **Extended Data Figure 8: Phenotypic characterisation of endothelial cells in**
1265 **healthy and cirrhotic human livers.**

1266 **a**, Clustering and selected genes expressed in 8,020 endothelial cells from 4 healthy and
1267 3 cirrhotic human livers. **b**, Scaled gene expression of endothelial cluster markers
1268 across endothelial cells from healthy (n=4) and cirrhotic (n=3) livers. **c**, Digital pixel
1269 quantification: PLVAP immunostaining of cirrhotic liver sections (n=10) in
1270 parenchymal nodules *versus* fibrotic septae (top), Wilcoxon two-tailed. ACKR1
1271 immunostaining of cirrhotic liver sections (n=10) in parenchymal nodules *versus*
1272 fibrotic septae (bottom), Wilcoxon two-tailed. **d**, Flow cytometry: endothelial cells
1273 from healthy (n=3, grey) or cirrhotic (n=7, red) livers, representative histogram for
1274 stated marker (top), mean fluorescence intensity (MFI, bottom), Mean±SEM, Mann-
1275 Whitney two-tailed. **e**, Flow-based adhesion assay: peripheral blood monocytes
1276 assessed for adhesion (top) and % of adherent cells which transmigrate (bottom);
1277 endothelial cells from healthy (n=5) or cirrhotic (n=4) livers, Mean±SEM, Mann-
1278 Whitney two-tailed. **f**, Endothelial cell gene knockdown: cirrhotic endothelial cells
1279 treated with siRNA to PLVAP (n=6), ACKR1 (n=5) or control siRNA (n=6).
1280 Representative flow cytometry histograms for stated marker (top); comparison to
1281 isotype control antibody. Flow-based adhesion assay (bottom), peripheral blood
1282 mononuclear cells assessed for adhesion (bottom left) and % of adherent cells which
1283 transmigrate (bottom right) following siRNA treatment of endothelial cells,
1284 Mean±SEM, Kruskal-Wallis and Dunn. **g**, Self-Organising Map (SOM; 60 x 60 grid;
1285 top left): smoothed scaled metagene expression of endothelia lineage. 21,237 genes,
1286 3,600 metagenes, 45 signatures. A-E label metagene signatures overexpressed in one
1287 or more endothelial subpopulations. SOM: smoothed mean metagene expression profile
1288 for each endothelial subpopulation (bottom left). Radar plots (middle): metagene
1289 signatures A-E showing distribution of signature expression across endothelial
1290 subpopulations, exemplar genes (middle) and Gene Ontology (GO) enrichment (right),
1291 Fisher's exact test. **h**, Heatmap: endothelial subpopulation transcription factor regulon
1292 expression (colour coded top by cluster and condition) across 8,020 endothelial cells
1293 from 4 healthy and 3 cirrhotic human livers. Exemplar regulons labelled right. Cells in
1294 columns, regulons in rows. **i**, t-SNE visualisation, endothelial lineage (8,020 cells from
1295 healthy (n=4) and cirrhotic (n=3)), annotating *monocle* pseudotemporal dynamics

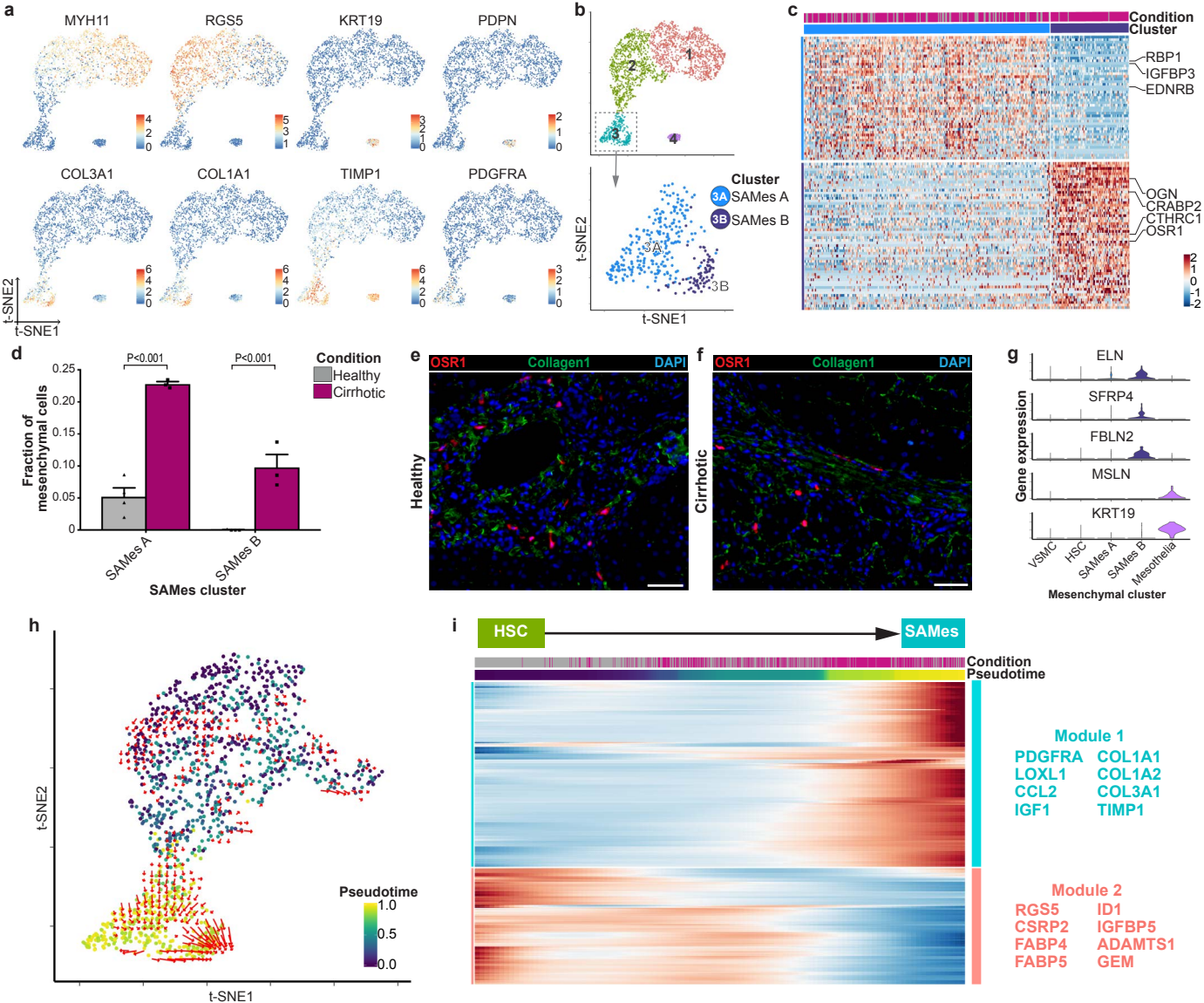
1296 (purple to yellow; grey indicates lack of inferred trajectory). RNA velocities (red
1297 arrows) visualised using Gaussian smoothing on regular grid. (purple to yellow). **j**,
1298 Representative immunofluorescence images healthy *versus* cirrhotic liver: RSPO3,
1299 PDPN, AIF1L, VWA1 or ACKR1 (red), CD34 (white), PLVAP (green), DAPI (blue),
1300 scale bars, 50µm. **k**, Annotation of 8,020 endothelial cells by subpopulation and injury
1301 condition. LSEC, Liver sinusoidal endothelial cells.



1302 **Extended Data Figure 9: Characterisation of mesenchymal cells in healthy and**
1303 **cirrhotic human livers.**

1304 **a**, Selected genes expressed in 2,318 mesenchymal cells from 4 healthy and 3 cirrhotic
1305 human livers. **b**, Clustering 319 scar-associated mesenchymal cells (SAMes) into 2
1306 further subclusters. **c**, Heatmap: SAMes subcluster marker genes (top, colour coded by
1307 cluster and condition), exemplar genes labelled (right). Cells columns, genes rows. **d**,
1308 Fractions of SAMes subpopulations in healthy (n=4) *versus* cirrhotic (n=3) livers,
1309 Mean±SEM, Wald. **e**, Representative immunofluorescence image, portal region of
1310 healthy liver: OSR1 (red), Collagen 1 (green), DAPI (blue), Scale bar 50µm. **f**,
1311 Representative immunofluorescence image, fibrotic niche of cirrhotic liver: OSR1
1312 (red), Collagen 1 (green), DAPI (blue), Scale bar 50µm. **g**, Scaled gene expression of
1313 selected genes across 2,318 mesenchymal cells from healthy (n=4) and cirrhotic (n=3)
1314 livers. **h**, t-SNE visualisation, 1,178 Hepatic Stellate Cells (HSC) and SAMes from
1315 healthy (n=4) and cirrhotic (n=3) livers annotated by *monocle* pseudotemporal
1316 dynamics (purple to yellow). RNA velocity field (red arrows) visualised using Gaussian
1317 smoothing on regular grid. **i**, Heatmap: cubic smoothing spline curves fitted to genes
1318 differentially expressed across HSC-to-SAMes pseudotemporal trajectories, grouped
1319 by hierarchical clustering (k=2). Colour coded by pseudotime and condition (top). Gene
1320 co-expression modules (colour) and exemplar genes labelled right.

1321



1322 **Extended Data Figure 10: Characterisation of the cellular interactome in the**
1323 **fibrotic niche.**

1324 **a to b**, Representative immunofluorescence images, fibrotic niche cirrhotic liver. **a**,
1325 TREM2 (red), PLVAP (white), PDGFR α (green), DAPI (blue), Scale bars 50 μ m. **b**,
1326 TREM2 (red), ACKR1 (white), PDGFR α (green), DAPI (blue), Scale bars 50 μ m. **c**,
1327 Proliferation assay: Human hepatic stellate cells (HSC) treated with conditioned media
1328 from primary hepatic macrophage subpopulations SAM Φ (n=2), tissue monocytes
1329 (TMo, n=2), Kupffer cells (KC, n=2) or control media (n=2). y-axis, area under curve
1330 (AUC) of % change in HSC number over time (hours), Mean \pm SEM. **d**, Circle plot:
1331 potential interaction magnitude from ligands expressed by scar-associated macrophages
1332 (SAM Φ) and endothelial cells (SAEndo) to receptors expressed on scar-associated
1333 mesenchyme (SAMes). **e**, Circle plot: potential interaction magnitude from ligands
1334 expressed by SAMes to receptors expressed on SAM Φ and SAEndo. **f**, Dotplot: ligand-
1335 receptor interactions between SAMes (n=7 human livers), SAM Φ (n=10 human livers)
1336 and SAEndo (n=7 human livers). X-axis, ligand (red) and cognate receptor (blue); y-
1337 axis, ligand (red) and receptor (blue) expressing cell populations; circle size, P value
1338 (permutation test); colour (red, high; yellow, low), means of average ligand and
1339 receptor expression levels in interacting subpopulations. **g**, Representative
1340 immunofluorescence images, fibrotic niche in cirrhotic liver. Top; CCL2 (red), CCR2
1341 (white), PDGFR α (green), DAPI (blue), arrows CCL2⁺PDGFR α ⁺ cells. Bottom;
1342 ANGPT1 (red), TEK(white), PDGFR α (green), DAPI (blue), arrows
1343 ANGPT1⁺PDGFR α ⁺ cells. Scale bars 50 μ m. **h**, Circle plot: potential interaction
1344 magnitude from ligands expressed by to receptors expressed on SAEndo. **i**, Dotplot:
1345 ligand-receptor interactions between SAM Φ (n=10 human livers) and SAEndo (n=7
1346 human livers). X-axis, ligand (red) and cognate receptor (blue); y-axis, ligand (red) and
1347 receptor (blue) expressing cell populations; circle size, P value (permutation test);
1348 colour (red, high; yellow, low), means of average ligand and receptor expression levels
1349 in interacting subpopulations. **j**, Representative immunofluorescence image, fibrotic
1350 niche in cirrhotic liver. TREM2 (red), FLT1 (white), VEGFA (green), DAPI (blue),
1351 arrows TREM2⁺VEGFA⁺ cells, Scale bar 50 μ m. **k**, Circle plot: potential interaction
1352 magnitude from ligands expressed by SAEndo to receptors expressed on SAM Φ . **l**,
1353 Dotplot: ligand-receptor interactions between SAEndo (n=7 human livers) and SAM Φ

1354 (n=10 human livers). X-axis, ligand (red) and cognate receptor (blue); y-axis, ligand
1355 (red) and receptor (blue) expressing cell populations; circle size, P value (permutation
1356 test); colour (red, high; yellow, low), means of average ligand and receptor expression
1357 levels in interacting subpopulations. **m**, Representative immunofluorescence images,
1358 fibrotic niche in cirrhotic liver. Top; TREM2 (red), CD200 (white), CD200R (green),
1359 DAPI (blue), arrows TREM2⁺CD200R⁺ cells. Bottom; TREM2 (red), DLL4 (white),
1360 NOTCH2 (green), DAPI (blue), arrows TREM2⁺NOTCH2⁺ cells. Scale bars, 50µm.
1361

